Eidgenössische Technische Hochschule Zürich

Ecole polytechnique fédérale de Zurich
Politecnico federale di Zurigo
Swiss Federal Institute of Technology Zurich

On the role of Riemann solvers in discontinuous Galerkin methods for magnetohydrodynamics

V. Wheatley*, P. Huguenot and H. Kumar

Research Report No. 2009-39
December 2009

Seminar für Angewandte Mathematik
Eidgenössische Technische Hochschule
CH-8092 Zürich
Switzerland

*School of Mechanical and Mining Engineering, The University of Queensland, Australia

On the Role of Riemann Solvers in Discontinuous Galerkin Methods for Magnetohydrodynamics

V. Wheatley[a], H. Kumar[b], P. Huguenot[b]

[a] *School of Mechanical and Mining Engineering, The University of Queensland, Australia*
[b] *Seminar for Applied Mathematics, ETH Zurich, Switzerland*

Abstract

It has been claimed that the particular numerical flux used in Runge-Kutta Discontinuous Galerkin (RKDG) methods does not have a significant effect on the results of high-order simulations. We investigate this claim for the case of compressible ideal magnetohydrodynamics (MHD). We also address the role of limiting in RKDG methods.

For smooth nonlinear solutions, we find that the use of a more accurate Riemann solver in third-order simulations results in lower errors and more rapid convergence. However, in the corresponding fourth-order simulations we find that varying the Riemann solver has a negligible effect on the solutions.

In the vicinity of discontinuities, we find that high-order RKDG methods behave in a similar manner to the second-order method due to the use of a piecewise linear limiter. Thus, for solutions dominated by discontinuities, the choice of Riemann solver in a high-order method has similar significance to that in a second-order method. Our analysis of second-order methods indicates that the choice of Riemann solver is highly significant, with the more accurate Riemann solvers having the lowest computational effort required to obtain a given accuracy. This allows the error in fourth-order simulations of a discontinuous solution to be mitigated through the use of a more accurate Riemann solver.

We demonstrate the the minmod limiter is unsuitable for use in a high-order RKDG method. It tends to restrict the polynomial order of the trial space, and hence the order of accuracy of the method, even when this is not needed to maintain the TVD property of the scheme.

Key words: Riemann solvers, discontinuous Galerkin methods, limiters
PACS: 52.30.Cv, 52.65.-y, 47.11.-j, 47.40.-x

1. Introduction

To simulate compressible flows that contain shocks along with small-scale features such as turbulence, we require numerical methods that are shock capturing, but also exhibit high-order accuracy and low numerical dissipation away from shocks [1]. Runge-Kutta Discontinuous Galerkin (RKDG) methods are

shock capturing and high-order accurate away from discontinuities, thus they are a candidate method for carrying out simulations.

Discontinuous Galerkin (DG) methods were first introduced by Hill and Reed [2] for the neutron transport equations (linear hyperbolic equations). LeSaint and Raviart [3] proved a rate of convergence of $O(\Delta x)^k$ for general triangulations and of $O(\Delta x)^{k+1}$ for Cartesian meshes, where Δx is the element size and k is the polynomial order of the approximate solution. In case of general triangulations, this result was then improved by Johnson and Pitkaranta [4] to $O(\Delta x)^{k+1/2}$, which was confirmed to be optimal by Peterson [5].

These methods were then generalized for systems of hyperbolic conservation laws by Cockburn et al. ([6], [7], [8], [9], [10]). In space the solution is approximated using piecewise polynomials on each element. Exact or approximate Riemann solvers from finite volume methods are used to compute the numerical fluxes between elements. Limiters are used to achieve non-oscillatory approximate solutions, if they contain shocks [11]. For these reasons, DG methods can be seen as generalization of finite volume methods to higher order. For time integration, the total variation diminishing (TVD) explicit Runge-Kutta (RK) methods proposed by Shu and Osher [12] are used.

RKDG methods have many important advantages. Like finite element methods, RKDG methods are well suited for simulating flows in complicated geometries. These methods can easily handle adaptivity strategies, because of the assumed discontinuity of the solution at element interfaces. This allows refining or unrefining of the triangulation to be done without taking into account the continuity restrictions typical of conforming finite element methods. Similarly, the degree of the polynomial approximation within an element can be changed without affecting the solution on other elements. Another important advantage is that these methods are highly parallelizable because to update the solution on a given element, only information from elements with which it shares a face is needed.

At present, it is believed that the particular numerical flux or Riemann solver used does not have a significant effect on the results of high-order RKDG simulations [13]. Such a conclusion is supported by numerical evidence such as that shown in Figure 1. This figure shows the results of simulations of the MHD shock tube problem described in Section 4.2 with three different flux calculators (see Section 4 for descriptions), along with the exact solution to the problem. The results of first- and second-order simulations are shown in Figures 1(a) and 1(b), respectively. Comparing these results, it appears that the absolute error in the numerical solution is far less sensitive to the choice of numerical flux when the second-order scheme is used. This seems to indicate that as the order of a simulation increases, the choice of numerical flux becomes less significant. This view has lead to the simple and highly dissipative Lax-Friedrichs (LF) flux being used within many RKDG methods [13]. Our goal is to rigorously examine the effect of more accurate numerical flux calculators in high-order RKDG methods, with particular emphasis on high-order simulations featuring discontinuities. The influence of accurate flux calculators in high-order RKDG methods is intimately tied to the performance of the limiters in

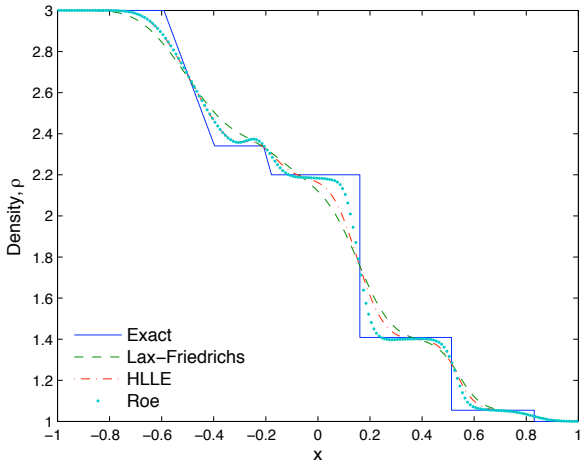

(a)

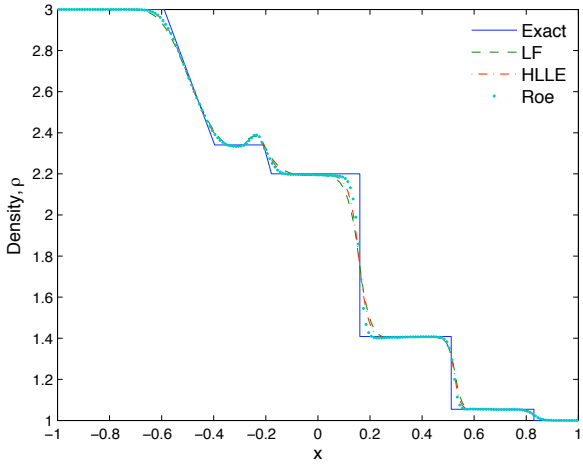

(b)

Figure 1: Density profiles at $t = 0.4$ from (a) first-order and (b) second-order accurate simulations of the MHD shock tube problem described in Section 4.2. The exact solution to the problem is shown along with numerical results using the LF, HLLE and Roe fluxes described in Section 4.

the method. For this reason, we also examine the performance of limiters in high-order simulations.

For the Euler equations, the effect of Riemann solvers has been previously evaluated by Qiu et al. [14]. One and two dimensional numerical simulations were carried out to compare various Riemann solvers based on performance measures such as numerical error, resolution of discontinuities and CPU times. The LF flux was shown to require the least CPU time among all the fluxes that were compared, but it also produced the largest numerical errors. Whereas second order fluxes such as Lax-Wendroff (LW) and Warming-Beam (WB) were found to be unstable. The Harten, Lax and van Leer (HLL) [15], HLLC [16] and MUSTA [17] fluxes were proposed as good choices for RKDG simulations. However, the data generated was not correlated to demonstrate which scheme is the most computationally efficient, or if the benefits of using more accurate Riemann solvers are dependent on the order of accuracy. In addition, error norms were only computed for a smooth linear problem, while we anticipate that the use of accurate Riemann solvers will be most significant in discontinuous nonlinear problems.

This report is organized as follows: In the next section we present the governing equations for the simulations. In Section 3 a brief description of the RKDG method is presented. In Section 4, a number of flux calculators for ideal MHD are tested, leading to the selection of appropriate flux calculators for use in the RKDG method in different circumstances. The limiters used within the RKDG method are described and tested in Section 5. The results of numerical test cases are presented and analyzed in Section 6. Finally, the conclusions that have been drawn from this work are presented in Section 7.

2. Governing equations

The governing equations for the simulations presented here are the ideal MHD equations. These govern the evolution of a quasi-neutral conducting fluid and the magnetic field within it, neglecting the magnetization of individual particles, the hall current, ion slip and the time rate of change of the electric field in Maxwell's equations. The complete details of their derivation may be found, for example, in Sutton and Sherman [18]. In the absence of viscosity, thermal conductivity, electrical resistivity and interspecies diffusion, the ideal

MHD equations are,

$$\frac{\partial \rho}{\partial t} + \nabla \cdot (\rho \mathbf{u}) = 0, \tag{1}$$

$$\rho \frac{D\mathbf{u}}{Dt} = -\nabla p + \frac{1}{\mu_0} (\nabla \times \mathbf{B}) \times \mathbf{B}, \tag{2}$$

$$\rho \frac{D}{Dt} \left(e + \frac{1}{2} \mathbf{u} \cdot \mathbf{u} \right) = -\frac{1}{\mu_0} (\nabla \times \mathbf{B}) \cdot (\mathbf{u} \times \mathbf{B}) - \nabla \cdot (p\mathbf{u}). \tag{3}$$

$$\nabla \cdot \mathbf{B} = 0, \tag{4}$$

$$\frac{\partial \mathbf{B}}{\partial t} = \nabla \times (\mathbf{u} \times \mathbf{B}) . \tag{5}$$

Here, ρ is the density, p is the pressure, $\mathbf{u}$ is the velocity, $\mathbf{B}$ is the magnetic field, e is the internal energy per unit mass and μ_0 is the magnetic permeability of vacuum. It is convenient to normalize $\mathbf{B}$ by $\sqrt{\mu_0}$, thus eliminating μ_0 from the system of equations.

Eqs. 1-5 can be written in conservation form as follows:

$$\frac{\partial U}{\partial t} + \frac{\partial F_j(U)}{\partial x_j} = 0, \tag{6}$$

where the vector of conserved variables $\mathbf{U} \equiv \mathbf{U}(x_i, t)$ is,

$$\mathbf{U} = \{\rho, \rho u_i, B_i, \rho e_T\}^T,$$

and the flux vectors $\mathbf{F}_j(\mathbf{U})$ are,

$$\mathbf{F}_j(\mathbf{U}) = \Big\{ \rho u_j \, , \, \rho u_i u_j + (p + \frac{1}{2} B_k B_k)\delta_{ij} - B_i B_j \, , \\ u_j B_i - u_i B_j \, , \, (\rho e_T + p + \frac{1}{2} B_k B_k) u_j - B_j (B_k u_k) \Big\}^T .$$

Here, ρe_T is the total energy per unit volume of the plasma. The plasma is assumed to be ideal with constant specific heats, allowing the following equation of state to be used to close the set of equations:

$$\rho e_T = \frac{p}{\gamma - 1} + \frac{1}{2} \rho u_k u_k + \frac{1}{2} B_k B_k.$$

3. Runge-Kutta Discontinuous-Galerkin Method

For hyperbolic problems, solutions may be piecewise continuous, meaning that they are smooth in regions separated by discontinuities. This behavior is mimicked by DG methods as they allow L^2 jumps at the boundaries of subdomains even for operators of higher than first order. This allows any complete set of trial functions to be used to represent the solution on each subdomain.

This is not the case in the standard Galerkin formulation where for second order operators, C^0 continuity is required across subdomains. RKDG methods for systems of hyperbolic conservation laws were developed by Cockburn et al. ([6], [7], [8], [9], [10]). For completeness, we present the following brief account of their derivation.

3.1. Variational Form

Consider a domain $\Omega \in \mathbb{R}^n$. Let us define a triangulation M of Ω as a finite collection $\{E_i\}_{i=1}^m, m \in \mathbb{N}$, of non-degenerate polygons such that,

$$\bar{\Omega} = \bigcup \{\bar{E}_i, i = 1, ..., m\}, \tag{7}$$

$$E_i \bigcap E_j = \emptyset \Leftrightarrow i \neq j, \tag{8}$$

and for all $i, j \in \{1, ..., m\}, i \neq j$, the intersection $\bar{E}_i \bigcap \bar{E}_j$ is either $\emptyset$ or a vertex, edge or face of both E_i and E_j. For two-dimensional quadrilateral elements, we introduce a reference element $\Sigma \equiv [-1, 1] \times [-1, 1]$ and the mapping,

$$\Phi : E \to \Sigma \tag{9}$$

that maps quadrilateral elements to the reference element. The mapping Φ is a bilinear mapping.

It is sufficient for us to consider the following generic scalar advection equation:

$$\frac{\partial u}{\partial t} + \nabla \cdot \boldsymbol{F} = 0, \tag{10}$$

where u is a conserved variable and $\boldsymbol{F}$ is the inviscid flux vector. The variational form used in the RKDG method is derived by multiplying by the test function v and integrating over each element separately. After using integration by parts on the divergence term, we obtain,

$$\int_E \frac{\partial u}{\partial t} v \, dx + \int_{\partial E} v \boldsymbol{n} \cdot \boldsymbol{F}(u) \, ds - \int_E \nabla v \cdot \boldsymbol{F}(u) \, dx = 0. \tag{11}$$

The flux vector $\boldsymbol{F}(u)$ in the second term must be evaluated on the boundary of the element where u may be discontinuous and thus has two possible values; u_i on the interior of the element under consideration and u_e on the exterior. To account for this, we replace $\boldsymbol{F}(u)$ with the numerical flux function $\hat{\boldsymbol{F}}(u_i, u_e)$, which can be computed taking upwind considerations into account. The final variational from is derived by using integration by parts once more on the third term to eliminate the gradient of the test function,

$$\frac{\partial}{\partial t} \int_E uv \, dx + \int_{\partial E} v \left(\hat{\boldsymbol{F}}(u_i, u_e) - \boldsymbol{F}(u_i) \right) \cdot \boldsymbol{n} \, ds + \int_E \nabla \cdot \boldsymbol{F}(u) v \, dx = 0. \tag{12}$$

3.2. Basis Functions

In the RKDG method, the unknowns and data within each element are expanded in terms of a suitable set of basis functions $\phi_{pq}(\boldsymbol{x})$;

$$f(x,y) = \sum_p \sum_q a_{pq}\phi_{pq}(\xi_1,\xi_2).$$

Here, (ξ_1,ξ_2) is a local coordinate system associated with that element. The RKDG method we use is based on the Nektar code by [19]. The original code has been extended to include Runge-Kutta time stepping, slope limiters and accurate Riemann solvers, amongst other features. We will refer to the modified version of the code as Nektar-m. The set of polynomial basis functions used in Nektar was proposed by [20] in two dimensions and extended to three dimensions in [19]. The two-dimensional basis functions have the form,

$$\phi_{pq}(\xi_1,\xi_2) = \psi_p^a(\xi_1)\psi_q^b(\xi_2),$$

for quadrilaterals and,

$$\phi_{pq}(\xi_1,\xi_2) = \psi_p^a(\eta_1)\psi_{pq}^b(\eta_2),$$

for triangles. The Cartesian coordinates ξ_1, ξ_2 are defined on the reference element as shown in Fig. 2, while η_1, η_2 are non-Cartesian and are given by,

$$\eta_1 = 2\frac{1+\xi_1}{1-\xi_2} - 1, \quad \eta_2 = \xi_2.$$

The functions $\psi_p^a(z)$ and $\psi_{pq}^b(z)$ are,

$$\psi_p^a(z) = P_p^{0,0}(z), \quad \psi_{pq}^b(z) = \left(\frac{1-z}{2}\right)^p P_q^{2p+1,0}(z),$$

where $P_n^{\alpha,\beta}$ is the nth-order Jacobi polynomial with weights α and β. These basis functions are orthogonal in the Legendre inner product over each element, resulting in a diagonal mass matrix. The functions are polynomial in both the Cartesian and non-Cartesian co-ordinates. It was proved by [21] that the coefficients of the basis functions in a solution decay exponentially with polynomial order, thus the numerical solution converges exponentially as the maximum polynomial order of the approximation is increased.

3.3. Runge-Kutta Time Discretization

To advance solutions in time, the RKDG method uses a Runge-Kutta (RK) time marching scheme. In this manuscript we present the results of second-, third- and fourth-order accurate RKDG schemes, thus we limit ourselves to presenting the RK schemes used in these cases. For second- and third-order simulations, we use the TVD RK schemes of [22]. For fourth-order simulations we use the classic scheme.

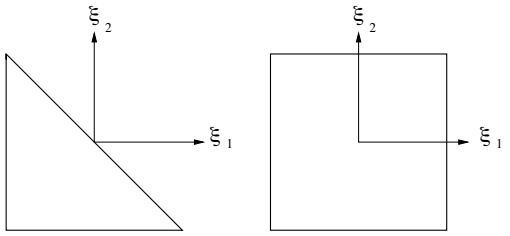

Figure 2: Reference element local coordinate system.

order	α_{il}			β_{il}		
2	1			1		
	1/2	1/2		0	1/2	
3	1			1		
	3/4	1/4		0	1/4	
	1/3	0	2/3	0	0	2/3

Table 1: Parameters for TVD Runge-Kutta time marching schemes.

Consider the semi-discrete ODE,

$$\frac{du_h}{dt} = L_h(u_h).$$

Let u_h^n be the discrete solution at time t^n, and let $\Delta t^n = t^{n+1} - t^n$. In order to advance a numerical solution from time t^n to t^{n+1}, the RK algorithm is as follows:

1. Set $u_h^{(0)} = u_h^n$.
2. For $i = 1, ..., k+1$, compute,

$$u_h^{(i)} = \sum_{l=0}^{i-1} \alpha_{il} u_h^{(l)} + \beta_{il} \Delta t^n L_h(u_h^{(l)}).$$

3. Set $u_h^{n+1} = u_h^{(k+1)}$.

The values of the coefficients used in the TVD schemes are shown in Table 3.3.

For the linear advection equation, it was proved by [23] that the RKDG method is L^∞-stable for piecewise linear ($k = 1$) approximate solutions if a second-order RK scheme is used with a time-step that satisfies,

$$c\frac{\Delta t}{\Delta x} \leq \frac{1}{3},$$

where c is the constant advection speed. The numerical experiments of [24] show that when approximate solutions of polynomial degree k are used, an

order $k+1$ RK scheme must be used, which simply corresponds to matching the temporal and spatial accuracy of the RKDG scheme. In this case the L^∞-stability condition is

$$c\frac{\Delta t}{\Delta x} \leq \frac{1}{2k+1}.$$

For the nonlinear case, the same stability conditions are used but with c replaced by the maximum wave speed of the system.

3.4. Algorithm

Here we describe the RKDG algorithm as it is implemented in Nektar-m. The majority of the algorithm remains unchanged from that presented in [21]. It utilizes two sets of quadrature points on element boundaries: The set of interface quadrature points Q^I, where a Riemann solver is used to compute the numerical fluxes, and the set of edge quadrature points Q^E, where the fluxes must be evaluated to advance the solution in time. Q^I corresponds to the Gauss quadrature points along each edge, which do not include the vertices where there are no clearly defined left and right states that could be input to the Riemann solver. The set Q^E depends on the type of elements used and typically includes the vertices. The basic steps in the RKDG algorithm implemented in Nektar-m are as follows:

1. Read in the initial condition $\boldsymbol{U}(\boldsymbol{x}, 0)$ and evaluate it at all quadrature points, set $n = 0$.

2. Limit the solution to ensure that the method is total variation bounded (TVB) (see Section 5).

3. Compute the numerical fluxes $\hat{\boldsymbol{F}}_n$ at Q^I using a Riemann solver (see Section 4). At the domain boundaries, use the prescribed boundary conditions as the exterior state that is input to the Riemann solver. Interpolate the resulting fluxes onto Q^E. Scale the fluxes with the ratio of the edge Jacobian to the volume Jacobian. This increases the efficiency of the scheme by allowing the fluxes to be added to the volume terms evaluated at the quadrature points (see [21] for details).

4. Compute the exact fluxes $\boldsymbol{F}$ at the element quadrature points. Utilizing the known gradients of the basis functions, $\nabla \cdot \boldsymbol{F}$ is readily computed via a mapping.

5. Subtract $\boldsymbol{F}$ from $\hat{\boldsymbol{F}}_n$ at the appropriate quadrature points and add this to the result of step 4.

6. Determine the modal coefficients of the result of step 5 by evaluating its inner product with each orthogonal basis function. Store the result in $\mathbf{Uf}$.

7. Carry out the first substep of the RK time integration scheme:

$$\boldsymbol{U}^{(1)} = \boldsymbol{U}(\boldsymbol{x}, t^n) + \beta_{10}\Delta t \mathbf{Uf}(\boldsymbol{x}, t^n).$$

8. Repeat steps 2 to 6 for the remaining substeps in the RK scheme.

9. Increment n by one and t^n by Δt. Continue steps 2 to 9 until the desired simulation time is reached.

4. MHD Riemann Solvers

Riemann solvers are essential components in finite volume (FV) or RKDG methods. The function of a Riemann solver is to compute the flux across an interface that initially separates two uniform states:

$$\mathbf{U}(x,0) = \begin{cases} \mathbf{U}_l, & x \leq c \\ \mathbf{U}_r, & x > c \end{cases}$$

where $c \in \mathbb{R}$. Such Riemann problems arise at the element boundaries of a computational grid at every timestep. In this context Riemann solvers may also be referred to as flux calculators. In recent years a wide variety of Riemann solvers have been developed for ideal MHD (see e.g. [25, 26, 27, 28, 29, 30]). Due to the number of solvers available, selection of the optimal solver for a given simulation is difficult. This issue was addressed by Wesenberg (2002), who assessed the computational time required to reach a fixed error bound for finite volume simulations of a suite of test cases using six different Riemann solvers. This was done for both first and second order accurate finite volume schemes. Wesenberg concluded that his MHD-HLLEM was the cheapest for achieving a fixed error bound. However, since the time of Wesenberg's paper, several attractive new Riemann solvers of the HLLC family have been developed for MHD [26, 27, 28, 29, 30]. Our goal here is to assess the performance of a selection these new schemes so that we may select the best for a more extensive testing in high-order RKDG methods. In particular we will compare the performance of the HLLC solvers of Li [28] (HLLC-L) and Gurski [29] (HLLC-G) with the HLLD solver of Miyoshi and Kusano [30], the Lax-Friedrichs (LF) flux, an MHD Roe solver [31], the HLLE solver [15, 32] and the MHD-HLLEM solver. We will use a different test case to Wesenberg (see Section 6) that more completely exercises the capabilities of the Riemann solvers. In addition to being accurate and efficient, we must also consider the robustness of these Riemann solvers. This issue has been addressed for a number of solvers by Gurski [33]. Physical solutions of the MHD equations possess a positivity preserving property such that positive densities and pressures are always retained. However, non-physical negative densities and pressures can be generated in numerical solutions. Thus it is important that the MHD Riemann solver selected leads to a positivity preserving scheme. The HLLE and HLLC family of Riemann solvers have the additional benefit that they can be simply extended to the case there the plasma is not an ideal gas, which is not the case with the Roe and HLLE-M solvers.

In this section we will first give an overview of the Riemann solvers evaluated here, then present the results of the test cases. We will then conclude the with selection of the optimal Riemann solvers to use in certain situations.

4.1. Description of Solvers

4.1.1. Lax-Friedrichs Flux

The Lax-Friedrichs flux is a simple numerical flux that is used in many RKDG methods. Only the exact flux $\mathbf{F}$ must be know to compute this flux:

$$\mathbf{g}_{lf}(\mathbf{U}_l, \mathbf{U}_r) = \frac{1}{2}\big(\mathbf{F}(\mathbf{U}_l) + \mathbf{F}(\mathbf{U}_r)\big) - \frac{\triangle x}{2\triangle t}(\mathbf{U}_r - \mathbf{U}_l). \tag{13}$$

4.1.2. Roe Solver

The Roe flux is computed from a local linearization of the system about what is known as the Roe average state $\hat{\mathbf{U}}$. The Roe average state should be selected such that the Roe matrix $\mathcal{A}(\mathbf{U}_l, \mathbf{U}_r) \equiv D\mathbf{F}(\hat{\mathbf{U}}(\mathbf{U}_l, \mathbf{U}_r))$ satisfies:

$$\mathbf{F}(\mathbf{U}_l) - \mathbf{F}(\mathbf{U}_r) = \mathcal{A}(\mathbf{U}_l, \mathbf{U}_r)(\mathbf{U}_l - \mathbf{U}_r).$$

The Roe flux is then given by:

$$\mathbf{g}_{roe}(\mathbf{U}_l, \mathbf{U}_r) = \frac{1}{2}\big(\mathbf{F}(\mathbf{U}_l) + \mathbf{F}(\mathbf{U}_r)\big) - \frac{1}{2}\Sigma_{j=1}^{7}|\lambda_j(\hat{\mathbf{U}})|\alpha_j \mathbf{r}_j(\hat{\mathbf{U}}), \tag{14}$$

where $\alpha_j = \mathbf{l}_j(\hat{\mathbf{U}})(\mathbf{U}_r - \mathbf{U}_l)$. Here $\mathbf{l}_j$ and $\mathbf{r}_j$ are the left and right eigenvectors of the ideal MHD system, respectively, that correspond to the eigenvalue λ_j. For $\gamma = 2$, the Roe average state for the ideal MHD equations is given by [34],

$$\hat{\rho} := \sqrt{\rho_l \rho_r}, \qquad \hat{u_i} := \frac{\sqrt{\rho_l}u_{il} + \sqrt{\rho_r}u_{ir}}{\sqrt{\rho_l} + \sqrt{\rho_r}}$$

$$\hat{H} := \frac{\sqrt{\rho_l}H_l + \sqrt{\rho_r}H_r}{\sqrt{\rho_l} + \sqrt{\rho_r}}, \qquad \hat{B_i} = \hat{B}\frac{\frac{B_{il}}{\sqrt{\rho_l}} + \frac{B_{ir}}{\sqrt{\rho_r}}}{\sqrt{\rho_l} + \sqrt{\rho_r}}$$

For general γ, construction of the Roe average state is much more complicated and has been pursued, for example, by [35] and [36]. In practice the arithmetic average state is used instead of the Roe average state for $\gamma \neq 2$, which has been shown to work well [31].

It must be noted that there are issues with the robustness of the Roe solver. It has been shown that any linearization of certain Riemann problems for the Euler equations results in negative densities and pressures, thus no linearized Riemann solver is guaranteed to be positivity preserving for the Euler equations [32]. For the MHD equations, linearized Riemann solvers become even more problematic as negative pressure may be produced by numerical error in the magnetic energy as well as the kinetic energy [30].

A further complication with the Roe solver arises if we choose to use the method of [37] to control divergence errors in the magnetic field. In this approach the MHD system is augmented with a RHS proportional to $\nabla \cdot \mathbf{B}$ in order to minimize divergence errors:

$$\frac{\partial \mathbf{U}}{\partial t} + \nabla \cdot \mathbf{F} = \mathbf{S} \quad \rightarrow \quad \frac{\partial \mathbf{U}}{\partial t} + \mathbf{A} \cdot \nabla \mathbf{U} = 0.$$

A Roe solver is then usually constructed based on the Eigensystem of $\mathbf{A}$. However, the usual expression for the Roe flux is no longer appropriate, as $\mathbf{A} \cdot \nabla \mathbf{U} \neq \nabla \cdot \mathbf{F}$ since $\mathbf{A} \cdot \nabla \mathbf{U}$ includes the source term. One approach to make the Roe solver consistent is to first decompose the jump in conserved variables into eigenmodes,

$$\alpha_j = \mathbf{l}_j(\mathbf{U}_R - \mathbf{U}_L),$$

then compute the upwind solution to the linearized Riemann problem using,

$$\mathbf{U}^* = \frac{1}{2}[\mathbf{U}_l + \mathbf{U}_r - \sum_{j=1}^{8} \text{sign}(\lambda_j)\alpha_j \mathbf{r}_j].$$

Finally, we obtain the numerical flux by substituting $\mathbf{U}^*$ into the exact expression for the flux:

$$\hat{\mathbf{F}} = \mathbf{F}(\mathbf{U}^*).$$

4.1.3. HLLE Solver

Across any wave propagating the velocity b and separating states $\mathbf{U}^*$ and $\mathbf{U}$, the Rankine-Hugoniot relations hold,

$$\mathbf{F}^* - \mathbf{F} = b(\mathbf{U}^* - \mathbf{U}) \tag{15}$$

The HLL Riemann solver [15] is constructed by assuming a solution that consists of a single intermediate state $\mathbf{U}^*$ between the fastest and slowest (most negative) waves. An expression for the intermediate state can be easily be derived from the RH relations,

$$\mathbf{U}_{hll} = \mathbf{U}^* = \frac{b_r \mathbf{U}_r - b_l \mathbf{U}_l - \mathbf{F}_r + \mathbf{F}_l}{b_r - b_l}, \tag{16}$$

where b_l and b_r are approximations of the minimum and maximum signal speeds, respectively. Applying the RH relations across the entire Riemann fan gives an expression for the intermediate flux, which is the HLL flux,

$$\mathbf{g}_{HLLE}(\mathbf{U}_l, \mathbf{U}_r) = \frac{b_r \mathbf{F}(\mathbf{U}_l) - b_l f\mathbf{F}(\mathbf{U}_r)}{b_r - b_l} + \frac{b_r b_l}{b_r - b_l}(\mathbf{U}_r - \mathbf{U}_l). \tag{17}$$

One highly effective choice of signal speed estimates is due to [32],

$$b_l = \min_i(\lambda_i(\mathbf{U}_l), \lambda_i(\mathbf{U}_m), 0) \text{ and } b_r = \max_i(\lambda_i(\mathbf{U}_r), \lambda_i(\mathbf{U}_m), 0)$$

where $\mathbf{U}_m$ is the Roe mean value. Then this choice of signal speeds is used, the solver is referred to as the HLLE solver. The HLLE solver is extremely robust as it is both positivity preserving [32] and satisfies and entropy inequality automatically [38]. However, due to the single intermediate state approximation, the HLLE solver cannot resolve non-fast isolated discontinuities, making it quite dissipative.

4.1.4. HLLEM Solver

The MHD HLLEM solver was developed by Wesenberg [25]. In this solver, an anti-diffusion term is added to the usual HLLE flux:

$$\mathbf{g}_{HLLEM} := g_{HLLE}(\mathbf{U}_l, \mathbf{U}_r) + a_0(\mathbf{U}_l, \mathbf{U}_r), \tag{18}$$

where,

$$a_0(\mathbf{U}_l, \mathbf{U}_r) = -\frac{b_r^+ b_l^-}{b_r^+ - b_l^-} \sum_{i=2}^{6} \delta_i \alpha_i r_i.$$

Here,

$$\delta_2 := \delta_6 := \delta_a, \quad \delta_3 := \delta_5 := \delta_s, \quad \delta_4 := \delta_e,$$

where,

$$\delta_e := \phi_1 \frac{v_f(v_m)}{v_f(v_m) + |u_x(v_m)|},$$

$$\delta_s := \phi_1 \frac{v_f(v_m)}{v_f(v_m) + (1-\phi_2)|u_x(v_m)| + v_s(v_m)},$$

$$\delta_e := \phi_1 \frac{v_f(v_m)}{v_f(v_m) + (1-\phi_2)|u_x(v_m)| + v_{ax}(v_m)},$$

$$\phi_1 := \Phi(v_f(v_m) - v_{ax}(v_m)),$$

$$\phi_2 := \Phi(B_x^2 + B_y^2(v_m) + B_z^2(v_m)),$$

and,

$$\Phi(x) = \begin{cases} 0, & \text{for } (x \in (-\infty, \epsilon)), \\ \frac{x-\epsilon}{\delta-\epsilon}, & \text{for } (x \in [\epsilon, \delta)), \\ 1, & \text{for } (x \in [\delta, \infty)). \end{cases}$$

4.1.5. HLLC Solvers

The HLLC family of solvers are derived by assuming an approximate solution to the Riemann problem in which the Riemann fan is separated into two intermediate states, $\mathbf{U}_l^*$ and $\mathbf{U}_r^*$, by a contact discontinuity. The normal velocity is assumed constant within the Riemann fan and is given by the HLL average (see Eq. 16),

$$u_{x_l}^* = u_{x_r}^* = \frac{(\rho u_x)_{hll}}{\rho_{hll}} \equiv u^* \tag{19}$$

The standard procedure in a HLLC solver is to then solve for the remainder of the intermediate states using the RH relations across each wave. For intermediate total pressure and densities, this yields,

$$p_{T_l}^* = p_{T_r}^* = p_{T_l} + \rho_l (b_l - u_{x_l})(u^* - u_{x_l}) \equiv p_T^*, \tag{20}$$

$$\rho_\alpha^* = \rho_\alpha \frac{b_\alpha - u_{x_\alpha}}{b_\alpha - u^*}, \tag{21}$$

where α can be l or r. [29] observed that when $B_x \neq 0$, the transverse magnetic field and velocity must be continuous across the contact (and therefore the entire

Riemann fan), in addition to the total pressure and normal velocity. These are then set to the HLL average,

$$u^*_{y_l} = u^*_{y_r} = \frac{(\rho u_y)_{hll}}{\rho_{hll}} \equiv u^*_y, \tag{22}$$

$$u^*_{z_l} = u^*_{z_r} = \frac{(\rho u_z)_{hll}}{\rho_{hll}} \equiv u^*_z, \tag{23}$$

$$B^*_{y_l} = B^*_{y_r} = B_{y_{hll}} \equiv B^*_y, \tag{24}$$

$$B^*_{z_l} = B^*_{z_r} = B_{z_{hll}} \equiv B^*_z \tag{25}$$

The following expression for the total energies of the intermediate states can then be derived from the RH relations:

$$e^*_\alpha = \frac{(b_\alpha - u_{x_\alpha})e_\alpha - p_{T_\alpha} u_{x_\alpha} + p^*_T u^* + B_x(\mathbf{u}_\alpha \cdot \mathbf{B}_\alpha - \mathbf{u}^* \cdot \mathbf{B}^*)}{b_\alpha - u^*}. \tag{26}$$

With the intermediate states completely determined, the intermediate fluxes $\mathbf{F}^*_\alpha$ are computed from the RH relations across the left and right waves. The numerical flux is then given by,

$$\mathbf{g}_{hllc} = \begin{cases} \mathbf{F}_l & \text{if } b_l > 0, \\ \mathbf{F}^*_l & \text{if } b_l \le 0 \le u_s, \\ \mathbf{F}^*_r & \text{if } u_s \le 0 \le b_r, \\ \mathbf{F}_r & \text{if } b_r < 0. \end{cases} \tag{27}$$

This is referred to as the HLLC-G flux. Note that this flux does not tend to the Euler HLLC flux in the limit of vanishing magnetic field. An alternative MHD HLLC solver was developed independently by [28], which is referred to as the HLLC-L solver. In this solver the following forms are used for the intermediate tangential velocities:

$$u^*_{y_\alpha} = u_{y_\alpha} + \frac{B_x(B_{y_\alpha} - B^*_y)}{\rho_\alpha(u^* - u_{x_\alpha})} \tag{28}$$

$$u^*_{z_\alpha} = u_{z_\alpha} + \frac{B_x(B_{z_\alpha} - B^*_z)}{\rho_\alpha(u^* - u_{x_\alpha})}. \tag{29}$$

These satisfy the RH relations over the entire Riemann fan, but not necessarily over the contact alone. This scheme does, however, have the property that it tends to the Euler HLLC flux in the limit of zero magnetic field [30].

4.1.6. HLLD Solver

In order to resolve more discontinuities exactly, [30] formulated a more complicated HLL type MHD Riemann solver in which the Riemann fan is assumed to consist of four intermediate states, $\mathbf{U}^*_l$, $\mathbf{U}^{**}_l$, $\mathbf{U}^{**}_r$, and $\mathbf{U}^*_r$, from left to right. These states are separated by an Alfvén wave, followed by the contact discontinuity, then another Alfvén wave, which have velocities b^*_l, u^*, and b^*_r, respectively. Similarly to the HLLC solver, the normal velocity is assumed constant

throughout the Riemann fan and is given by the HLL average, which explicitly is,

$$u^* = \frac{(b_r - u_{x_r})\rho_r u_{x_r} - (b_l - u_{x_l})\rho_l u_{x_l} - p_{T_r} + p_{T_l}}{(b_r - u_{x_r})\rho_r - (b_l - u_{x_l})\rho_l}. \tag{30}$$

The constant total pressure within the Riemann fan and ρ^*_α are given by Eq. 21, while the following expressions for the remaining variables in $\mathbf{U}^*_\alpha$ can be derived from the RH relations across the outermost waves:

$$u^*_{y_\alpha} = u_{y_\alpha} - B_x B_{y_\alpha} \frac{b_\alpha - u_{x_\alpha}}{\rho_\alpha (b_\alpha - u_{x_\alpha})(b_\alpha - u^*) - B_x^2} \tag{31}$$

$$B^*_{y_\alpha} = B_{y_\alpha} \frac{\rho_\alpha (b_\alpha - u_{x_\alpha})^2 - B_x^2}{\rho_\alpha (b_\alpha - u_{x_\alpha})(b_\alpha - u^*) - B_x^2} \tag{32}$$

$$u^*_{z_\alpha} = u_{z_\alpha} - B_x B_{z_\alpha} \frac{b_\alpha - u_{x_\alpha}}{\rho_\alpha (b_\alpha - u_{x_\alpha})(b_\alpha - u^*) - B_x^2} \tag{33}$$

$$B^*_{z_\alpha} = B_{z_\alpha} \frac{\rho_\alpha (b_\alpha - u_{x_\alpha})^2 - B_x^2}{\rho_\alpha (b_\alpha - u_{x_\alpha})(b_\alpha - u^*) - B_x^2} \tag{34}$$

$$e^*_\alpha = \frac{(b_\alpha - u_{x_\alpha})e_\alpha - p_{T_\alpha} u_{x_\alpha} + p^*_T u^* + B_x(\mathbf{u}_\alpha \cdot \mathbf{B}_\alpha - \mathbf{u}^* \cdot \mathbf{B}^*)}{b_\alpha - u^*}. \tag{35}$$

The inner states, $\mathbf{U}^{**}_\alpha$, are then computed from the RH relations for the Alfvén waves, which have propagation velocities,

$$b^*_l = u^* - \frac{|B_x|}{\sqrt{\rho^*_l}}, \quad b^*_r = u^* + \frac{|B_x|}{\sqrt{\rho^*_r}}. \tag{36}$$

Note that the density and total pressure are continuous across the Alfvén waves, while the magnetic field, velocity and total pressure are continuous across the contact, hence,

$$\rho^{**}_\alpha = \rho^*_\alpha, \tag{37}$$

$$p^{**}_{T_\alpha} = p^*_{T_\alpha}, \tag{38}$$

$$u^{**}_{y_l} = u^{**}_{y_r} \equiv u^{**}_y, \tag{39}$$

$$u^{**}_{z_l} = u^{**}_{z_r} \equiv u^{**}_z, \tag{40}$$

$$B^{**}_{y_l} = B^{**}_{y_r} \equiv B^{**}_y, \tag{41}$$

$$B^{**}_{z_l} = B^{**}_{z_r} \equiv B^{**}_z. \tag{42}$$

[30] obtained the following expressions for the remaining variables:

$$u^{**}_y = \frac{\sqrt{\rho^*_l} u^*_{y_l} + \sqrt{\rho^*_r} u^*_{y_r} + (B^*_{y_r} - B^*_{y_l})\mathrm{sign}(B_x)}{\sqrt{\rho^*_l} + \sqrt{\rho^*_r}}, \tag{43}$$

$$u^{**}_z = \frac{\sqrt{\rho^*_l} u^*_{z_l} + \sqrt{\rho^*_r} u^*_{z_r} + (B^*_{z_r} - B^*_{z_l})\mathrm{sign}(B_x)}{\sqrt{\rho^*_l} + \sqrt{\rho^*_r}}, \tag{44}$$

$$B^{**}_y = \frac{\sqrt{\rho^*_l} B^*_{y_l} + \sqrt{\rho^*_r} B^*_{y_r} + \sqrt{\rho^*_l \rho^*_r}(u^*_{y_r} - u^*_{y_l})\mathrm{sign}(B_x)}{\sqrt{\rho^*_l} + \sqrt{\rho^*_r}}, \tag{45}$$

$$B^{**}_z = \frac{\sqrt{\rho^*_l} B^*_{z_l} + \sqrt{\rho^*_r} B^*_{z_r} + \sqrt{\rho^*_l \rho^*_r}(u^*_{z_r} - u^*_{z_l})\mathrm{sign}(B_x)}{\sqrt{\rho^*_l} + \sqrt{\rho^*_r}}, \tag{46}$$

$$e^{**}_\alpha = e^{**}_\alpha \pm \sqrt{\rho^*_\alpha}(\mathbf{u}_\alpha{}^{**} \cdot \mathbf{B}_\alpha{}^{**} - \mathbf{u}_\alpha{}^{*} \cdot \mathbf{B}_\alpha{}^{*})\mathrm{sign}(B_x). \tag{47}$$

$$\tag{48}$$

The intermediate fluxes can then be obtained from the RH relations summed over multiple waves, for example,

$$\mathbf{F}_l^* = \mathbf{F}_l + b_l(\mathbf{U}_l^* - \mathbf{U}_l), \tag{49}$$

$$\mathbf{F}_l^{**} = \mathbf{F}_l + b_l^*\mathbf{U}_l^{**} - (b_l^* - b_l)\mathbf{U}_l^* - b_l\mathbf{U}_l. \tag{50}$$

In general the HLLD flux is given by,

$$\mathbf{g}_{hlld} = \begin{cases} \mathbf{F}_l & \text{if } b_l > 0, \\ \mathbf{F}_l^* & \text{if } b_l \le 0 \le b_l^*, \\ \mathbf{F}_l^{**} & \text{if } b_l^* \le 0 \le u^*, \\ \mathbf{F}_r^{**} & \text{if } u^* \le 0 \le b_r^*, \\ \mathbf{F}_r^* & \text{if } b_r^* \le 0 \le b_r, \\ \mathbf{F}_r & \text{if } b_r < 0. \end{cases} \tag{51}$$

This solver resolves isolated rotational discontinuities exactly, along with contact discontinuities, and reduces to the Euler HLLC solver when $B_x = 0$ [30]. Miyoshi and Kusano [30] also proved that the HLLD solver is positivity preserving (as are the HLLC solvers) if

$$b_l < u_{x_l} - \sqrt{\frac{\gamma - 1}{2\gamma}}c_{f_l}, \quad b_r > u_{x_r} + \sqrt{\frac{\gamma - 1}{2\gamma}}c_{f_r}, \tag{52}$$

which are clearly satisfied by the choice of signal speeds from the HLLE method.

4.2. Numerical Tests

The primary test case we have selected to evaluate the Riemann solvers described in the previous subsection is a shock tube problem from Torrilhon [39]. This shock tube problem was selected as it includes all types of admissible MHD waves (according to Falle and Komissarov [40]) within one solution: fast- and slow-mode rarefactions, rotational discontinuities, fast shocks and slow shocks. Thus it will thoroughly exercise the wave resolving capabilities of the Riemann solvers. Torrihon's shock tube problem is computed on the domain $-1 < x < 1$, $0 \le t \le 0.4$ with the following initial conditions:

$$(\rho,\, p,\, u,\, v,\, w,\, B_x,\, B_y,\, B_z) = \begin{cases} (3,\, 3,\, 0,\, 0,\, 0,\, 1.5,\, 1,\, 0), & x < 0 \\ (1,\, 1,\, 0,\, 0,\, 0,\, 1.5,\, \cos(1.5),\, \sin(1.5)), & x > 0 \end{cases}$$

The boundary conditions for the problem are extrapolated outflow at $x = \pm 1$, and periodicity in y. This test case is computed for an ideal plasma with $\gamma = 5/3$.

To facilitate comparison to published results (e.g. [25]), the Riemann solvers are tested within a standard finite volume method. First-order simulations use piecewise constant reconstruction in space and forward Euler time-stepping with a CFL number of 0.45. Second-order simulations use a MINMOD limited piecewise linear reconstruction in space and predictor-corrector time-stepping. For this test case we assess the performance of the schemes via the L^2-norm of

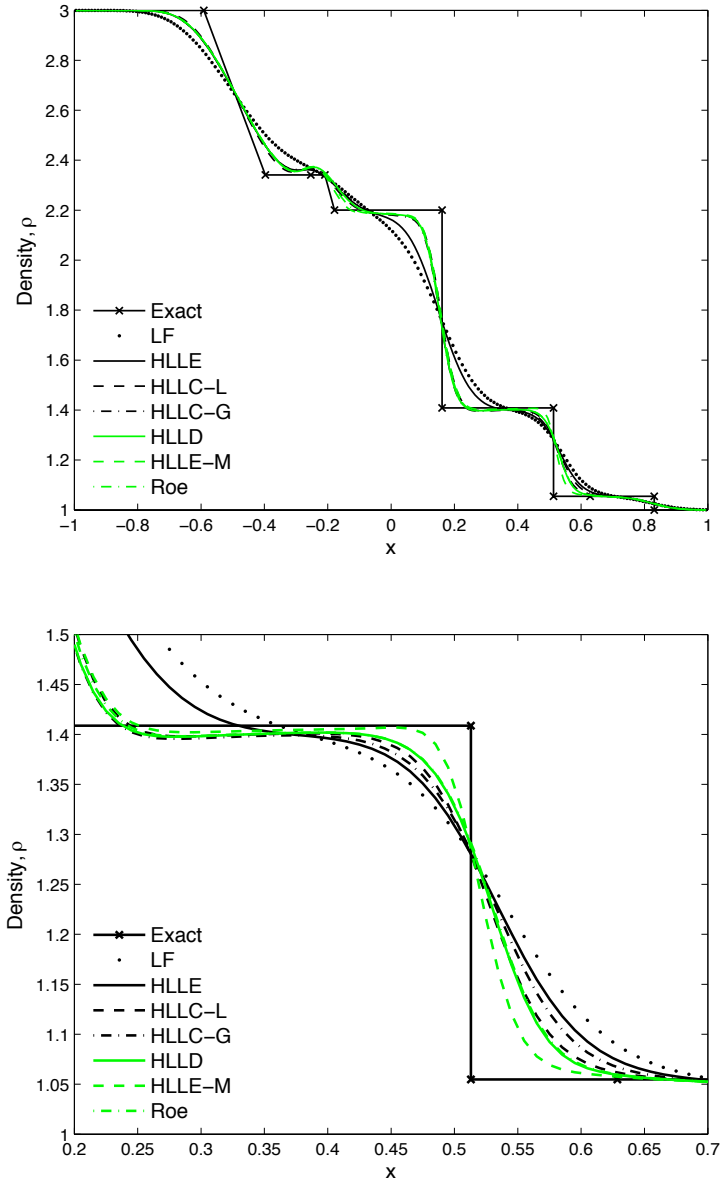

Figure 3: Density profiles at $t = 0.4$ from first-order solutions of Torrilhon's MHD shock tube problem on a grid of 200 cells using various Riemann solvers.

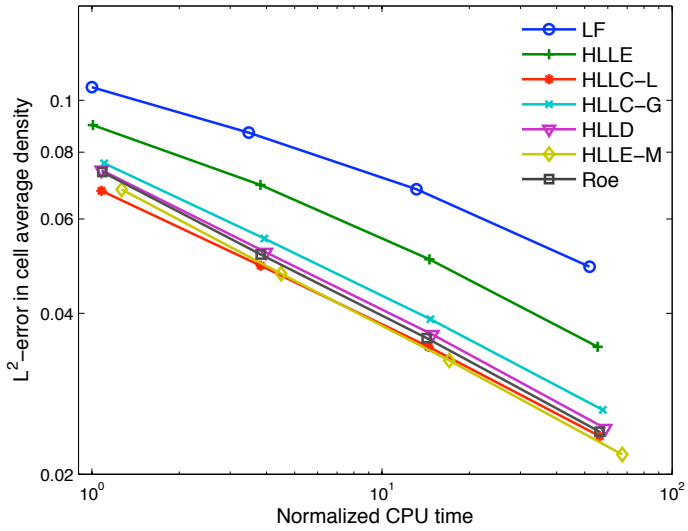

Figure 4: L^2-error in element average densities versus normalized CPU time for first-order simulations of Torrilhon's MHD shock tube problem on grids of 50, 100, 200, and 400 elements using various Riemann solvers.

the error in the cell averages, which in this case gives a measure of the scheme's overall ability to resolve discontinuities, and the CPU-time required to simulate the problem up until the final time, $T = 0.4$.

Figure 3 shows an example of the results of this test case. It shows the final density profiles produced by first-order finite volume simulations on a grid of 200 cells, along with the exact solution. Examining the density allows us to observe the performance of the schemes in the vicinity of the contact discontinuity, where the velocity and magnetic field do not vary. It does not, however, show the rotational discontinuities as these do not alter the density. In terms of resolution of discontinuities on a fixed grid, the Riemann solvers can be divided into three groups; the LF flux which is highly dissipative, the Roe, HLLC, HLLD, and HLLE-M solvers which capture all the discontinuities reasonably well even on this coarse grid, and the HLLE solver, which lies in between. In the first frame of Fig. 3, there appears to be little difference between the most accurate group of solvers. The second frame shows the solutions around the slow shock in greater detail. This allows us to see that the HLLD solution lies closest to the Roe solution, while the HLLE-M solution is even sharper (the shock is smeared over fewer cells) than Roe solution around the slow shock, due to the action of the anti-diffusion terms in the HLLE-M solver.

To assess the performance of the schemes more rigorously, we plot the L^2-norms of the error in element average density versus the computational effort (normalized CPU time) in Fig. 4. Curves that lie lower on this plot require

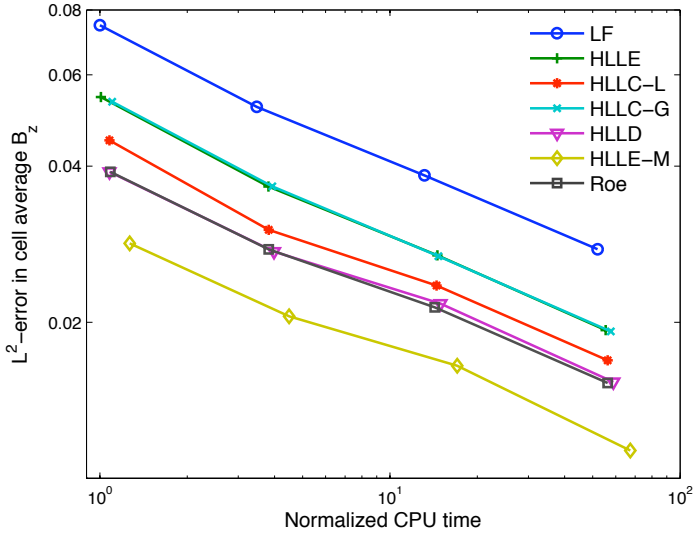

Figure 5: L^2-error in element average B_z versus normalized CPU time for first-order simulations of Torrilhon's MHD shock tube problem on grids of 50, 100, 200, and 400 elements using various Riemann solvers.

less computation effort to reach a fixed error bound, and are therefore said to perform better. From Fig. 4 we see that the LF-flux has the worst performance, followed by the HLLE solver. The performance of the HLLC-L, HLLC-G, HLLD, HLLE-M and Roe solvers is very similar, with HLLC-L and HLLE-M being the best for this performance measure at different resolutions, followed by HLLD, Roe, then HLLC-G. These rankings appear to be reasonably independent of resolution. Note, however, that the error in density does not assess the performance of the schemes around the rotational discontinuities, where we expect the HLLD and Roe solvers to be superior. To address this problem, in Fig. 5 we present the L^2-norms of the error in cell average B_z versus the CPU-time for the first-order simulations. From this figure, we see that for this performance measure the Roe, HLLE-M and HLLD solvers are superior to the HLLC solvers, with the HLLE-M solver requiring the minimum computational effort to achieve a given error bound.

In Fig. 6, we plot error norms versus the computational effort for second-order accurate simulations. The ordering of the schemes in terms of computational efficiency is mostly unchanged from the first-order results. The main exception is that the performance of the Roe, HLLD, HLLE-M, and HLLC-L solvers is practically identical.

So far we have assessed the accuracy and efficiency of our set of Riemann solvers. The robustness of the Riemann solvers is another important consideration. There are no known issues with the robustness of HLLE and HLLC-type

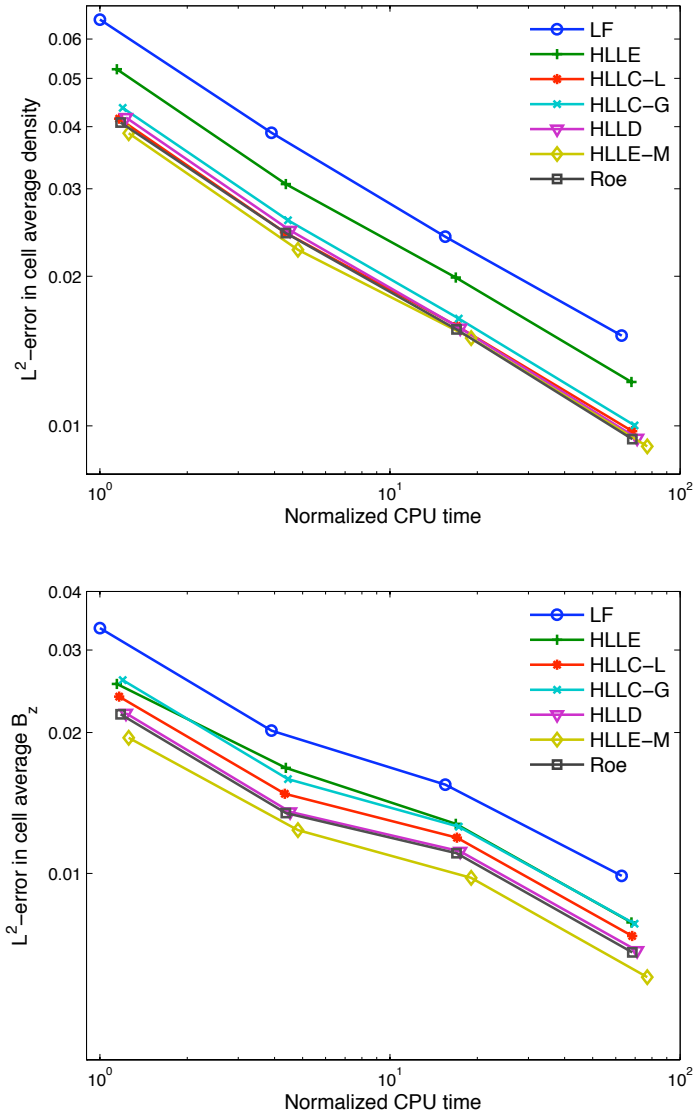

Figure 6: L^2-error in element average ρ (top) and B_z (bottom) versus normalized CPU time for second-order simulations of Torrilhon's MHD shock tube problem on grids of 50, 100, 200, and 400 cells using various Riemann solvers.

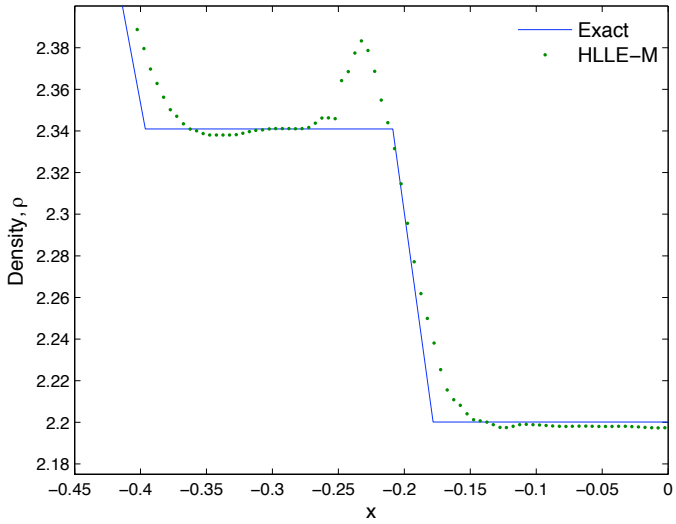

Figure 7: Partial density profile at $t = 0.4$ from second-order solutions of Torrilhon's MHD shock tube problem on a grid of 400 cells using the HLLE-M Riemann solver.

Riemann solvers, provided appropriate estimates for the signal speeds are used. There are however, multiple issues with the robustness of the Roe solver. In addition to the fact that the solver is not guaranteed to be positivity preserving [32], in multiple dimensions it has also been shown to produce what is known as the carbuncle phenomenon [41] when used to simulate shocks that are nearly stationary on the grid.

From the results presented so far, the HLLE-M solver appears to be the optimal choice of solver as it is gives the lowest error for a given computational cost. The source of the low error is the anti-diffusion terms in the solver. These cause the numerical representation of the discontinuities in the solution to be more sharply resolved than when the other solvers are used. This increased sharpness comes at a cost, however, as it results in the scheme being "over-compressive" which can lead to oscillations in the vicinity of discontinuities. Such oscillations are seen in the results of second-order accurate finite volume simulations, an example of which is shown in Fig. 7.

4.3. Selection of Solvers

From the results presented in this section, the optimal choices of Riemann solver appears to be the MHD HLLD solver of Miyoshi and Kusano [30] or the HLLC-L solver of Li [28]. These solvers exhibit high computational efficiency and have similarly low numerical dissipation to the Roe solver, but do not suffer from the same robustness issues. They are not as computationally efficient as the MHD HLLE-M solver, in terms of the error in the magnetic field, but we

observe that they do not generate numerical oscillations around discontinuities that we see when the HLLE-M solver is used. Additionally, both solvers have the property that they reduce to the Euler HLLC solver when the magnetic field vanishes, unlike the HLLC-G solver.

The HLLD solver requires slightly less computational effort than HLLC-L to produce the same error in the magnetic field, but the latter has the advantage that it is easier to implement. For this reason, we use the HLLC-L solver in our high-order RKDG simulations. In Section 6 we examine the impact of using this accurate Riemann solver in such simulations, compared to the LF flux.

5. Limiters

In order for the RKDG method to be stable in the nonlinear case, we require an entropy inequality and the uniform boundedness of the total variation of the discrete solution u_h [24]. In general, a limiter function is required for the second condition to hold. We present the limiter functions used in the RKDG method in the context of a one-dimensional nonlinear scalar equation. In order for the total variation of the means to be non-increasing for a forward Euler timestep, the discrete solution must satisfy (see [24] for details):

$$sign(\bar{u}_{j+1} - \bar{u}_j) = sign(p_{j+1/2}(u_h|E_{j+1}) - p_{j+1/2}(u_h|E_j)), \tag{53}$$

$$sign(\bar{u}_j - \bar{u}_{j-1}) = sign(u^-_{j+1/2} - u^-_{j-1/2}), \tag{54}$$

$$sign(\bar{u}_{j+1} - \bar{u}_j) = sign(u^+_{j+1/2} - u^+_{j-1/2}), \tag{55}$$

where $\bar{u}_j$ is the average solution on element E_j, $u^-_{j+1/2}$ denotes the limit of the solution at edge $j + 1/2$ taken from the left, $u^+_{j+1/2}$ denotes the limit of the solution at edge $j + 1/2$ taken from the right and,

$$p_{j+1/2}(u_h|E_{j+1}) = \bar{u}_j - \frac{\Delta t}{\Delta_{j+1}} f^+(u^-_{j+1/2}) + \frac{\Delta t}{\Delta_j} f^-(u^+_{j-1/2}).$$

Here, Δt is the forward Euler timestep, Δ_j is the size of E_j and we assume that the flux can be written in the form,

$$F(a, b) = f^+(a) + f^-(b),$$

which can be done for the Enquist-Osher flux, for example. There is no guarantee that the numerical solution will satisfy Eq. 53-Eq. 55, thus it is necessary to enforce them by means of what [24] refers to as a generalized slope limiter. These alter the numerical solution on an element in such a way that Eq. 53-Eq. 55 are satisfied, while preserving the element average of the solution and, as far as possible, the accuracy of the method.

Following the presentation of Cockburn [24], we will first review TVDM generalized slope limiters for the one-dimensional case, then show how these were modified to obtain schemes which are total variation bounded in the means (TVBM). We will then present the extension of these limiters to the two-dimensional case.

5.1. One-dimensional TVDM generalized slope limiters

A simple set for sufficient conditions on u_h that imply Eq. 53-Eq. 55 are satisfied can be stated in terms of the minmod function m,

$$m(a_1, ..., a_n) = \begin{cases} s \min_{1 \leq n \leq N} |a_n|, & \text{if } s = \text{sign}(a_1) = ... = \text{sign}(a_N) \\ 0, & \text{otherwise.} \end{cases}$$

It can be easily shown (see e.g. [24]) that Eq. 53-Eq. 55 are satisfied if, for all $j = 1, ..., N$, we have,

$$u^-_{j+1/2} - \bar{u}_j = m(u^-_{j+1/2} - \bar{u}_j, \bar{u}_j - \bar{u}_{j-1}, \bar{u}_{j+1} - \bar{u}_j), \tag{56}$$

$$\bar{u}_j - u^+_{j-1/2} = m(\bar{u}_j - u^+_{j-1/2}, \bar{u}_j - \bar{u}_{j-1}, \bar{u}_{j+1} - \bar{u}_j). \tag{57}$$

In the following, let v_h denote the numerical solution prior to limiting, and let Π_h denote the limiter. Thus the limited numerical solution is given by $u_h = \Pi_h(v_h)$. For the case of piecewise linear approximate solutions,

$$v_h|E_j = \bar{v}_j + (x - x_j)v'_j, \quad j = 1, ..., N,$$

we can apply slightly modified versions of the limiter functions from finite volume schemes. The generalized slope limiter based on the minmod limiter, Π^m_h, is,

$$u_h|E_j = \bar{v}_j + (x - x_j)m(v'_j, \frac{\bar{v}_{j+1} - \bar{v}_j}{\Delta_j}, \frac{\bar{v}_j - \bar{v}_{j-1}}{\Delta_j}). \tag{58}$$

This satisfies Eq. 56 and Eq. 57. The modification to the standard minmod limiter is the additional input of v'_j into the minmod function. The minmod generalized slope limiter is equivalent to,

$$u^-_{j+1/2} = \bar{v}_j + m(v^-_{j+1/2} - \bar{v}_j, \frac{\bar{v}_j - \bar{v}_{j-1}}{2}, \frac{\bar{v}_{j+1} - \bar{v}_j}{2}), \tag{59}$$

$$u^+_{j-1/2} = \bar{v}_j - m(\bar{v}_j - v^+_{j-1/2}, \frac{\bar{v}_j - \bar{v}_{j-1}}{2}, \frac{\bar{v}_{j+1} - \bar{v}_j}{2}). \tag{60}$$

Cockburn proposed the following less restrictive (LR) slope limiter, Π^{lr}_h, that also satisfies Eq. 56 and Eq. 57:

$$u_h|E_j = \bar{v}_j + (x - x_j)m(v'_j, \frac{\bar{v}_{j+1} - \bar{v}_j}{\Delta_j/2}, \frac{\bar{v}_j - \bar{v}_{j-1}}{\Delta_j/2}). \tag{61}$$

Compared to the minmod limiter, the LR limiter permits larger values of the internal gradient on an element before limiting occurs. As limiting decreases the accuracy of the solution on an element, this implies that use of the LR limiter will produce more accurate results. The LR slope limiter is equivalent to,

$$u^-_{j+1/2} = \bar{v}_j + m(v^-_{j+1/2} - \bar{v}_j, \bar{v}_j - \bar{v}_{j-1}, \bar{v}_{j+1} - \bar{v}_j), \tag{62}$$

$$u^+_{j-1/2} = \bar{v}_j - m(\bar{v}_j - v^+_{j-1/2}, \bar{v}_j - \bar{v}_{j-1}, \bar{v}_{j+1} - \bar{v}_j). \tag{63}$$

Both the minmod and the LR limiter are defined for piecewise linear solutions. They cannot be directly applied to solutions of higher polynomial order as $v_h'|E_j$ is in general non-constant. Instead, the limiting procedure is broken into two stages: detection and truncation. To detect if an element requires limiting the following procedure is used [24]:

1. Compute $u^+_{j-1/2}$ and $u^-_{j+1/2}$ using either Eq. 59 and Eq. 60 (minmod limiter) or Eq. 62 and Eq. 63 (LR limiter).
2. If $u^+_{j-1/2} = v^+_{j-1/2}$ and $u^-_{j+1/2} = v^-_{j+1/2}$, no limiting is required so set $u_h|E_j = v_h|E_j$, otherwise carry out the truncation stage.

In the truncation stage, we set $u_h|E_j$ equal to a limited lower order polynomial that satisfies Eq. 56 and Eq. 57. The simplest procedure is limiting to a piecewise constant by setting $u_h|E_j = \bar{v}_j$. We refer to this as the first-order limiter. The second-order limiter results from truncating $u_h|E_j$ to a piecewise linear function that satisfies Eq. 56 and Eq. 57. Following [24], this is done by applying Eq. 58 or Eq. 61 to the P^1 part of the solution,

$$v_h^1 = \sum_{l=0}^{1} \hat{v}_l \phi_l(x).$$

Thus $u_h|E_j = \Pi_h^m(v_h^1)$ or $u_h|E_j = \Pi_h^{lr}(v_h^1)$. It is important to note that this is more accurate than, for example, direct use Eq. 61 with $m(\frac{v^-_{j+1/2}-\bar{v}_j}{\Delta_j/2}, \frac{\bar{v}_j - v^+_{j-1/2}}{\Delta_j/2})$ as the first argument to the minmod function, which uses quantities already computed in the detection phase. The reason for this is that if limiting is needed due to the high-order modes only, then limiting v_h^1 will allow the original P^1 part of the solution to be preserved, while using the differences computed in the detection step will not.

5.2. One-dimensional TVBM generalized slope limiters

At local extrema, the solution is non-monotone thus any limiter based on the minmod function will limit the solution to a piecewise constant no matter how smooth the solution is. This results in a loss in accuracy at local extrema. Following [42], this can be avoided by replacing the minmod function in the limiters with the TVB corrected minmod function $\bar{m}$ which is defined as,

$$\bar{m}(a_1, ..., a_n) = \begin{cases} a_1, & \text{if } |a_1| \leq M\Delta x^2 \\ m(a_1, ..., a_n), & \text{otherwise,} \end{cases}$$

where M is a constant that is an upper bound for the absolute value of the curvature of the solution at local extrema. In this work, we take $M = 50$.

Provided that the value of M is appropriate, the scheme will not suffer from loss of accuracy at local extrema. The penalty for this is that the scheme is no longer TVD. It can, however, be shown to be total variation bounded in the

means (TVBM) [42]. Moreover, provided the CFL condition is satisfied and coefficients α_{il} from the Runge-Kutta scheme are nonnegative and satisfy,

$$\sum_{l=0}^{i-1} \alpha_{il} = 1,$$

then it can be shown to solutions produced by the RKDG scheme converge in the nonlinear case [24].

5.3. Two-dimensional TVBM generalized slope limiters

To extend the generalized slope limiters presented in the previous subsections to the multi-dimensional case, [10] relies on the assumption that spurious oscillations are present in u_h only if they are present in its P^1 part, u_h^1. Thus if,

$$u_h^1 = \Pi_h u_h^1, \tag{64}$$

indicating that limiting is not required for u_h^1, then it is assumed that that no limiting is required for the full solution u_h, hence,

$$\Pi_h u_h = u_h$$

Conversely, if limiting is required for u_h^1, the solution is truncated to the limited P^1 part,

$$\Pi_h u_h = \Pi_h u_h^1.$$

This approach has the drawback that it does not reduce to the one-dimensional scheme if the multi-dimensional scheme is applied to simulate a one-dimensional problem. In fact Eq. 56 and Eq. 57 are not guaranteed to be satisfied if only the P^1 part of the solution is used to detect where limiting is required. To demonstrate the implication of this (that the scheme is not TVD), in Fig. 8 we compare simulations of Torrilhon's MHD shock tube problem using the proposed multidimensional limiter and a scheme that does reduce to the one-dimensional LR limiter described above. We clearly see the appearance of spurious oscillation when only the P^1 part of the solution is used to detect where limiting is required.

The multi-dimensional limiter that we have utilized for rectangular discretizations uses Eq. 62 and Eq. 63 in each direction to detect whether limiting is required, with the exception that the point values at edges are replaced by edge average values. This has the advantage that it reduces to the one-dimensional scheme if it is used to simulate a one-dimensional problem. In detail, we compute,

$$\bar{u}^-_{i,j+1/2} = \bar{v}_{i,j} + \bar{m}(\bar{v}^-_{i,j+1/2} - \bar{v}_{i,j}, \bar{v}_{i,j} - \bar{v}_{i,j-1}, \bar{v}_{i,j+1} - \bar{v}_{i,j}), \tag{65}$$

$$\bar{u}^+_{i,j-1/2} = \bar{v}_{i,j} - \bar{m}(\bar{v}_{i,j} - \bar{v}^+_{i,j-1/2}, \bar{v}_{i,j} - \bar{v}_{i,j-1}, \bar{v}_{i,j+1} - \bar{v}_{i,j}). \tag{66}$$

$$\bar{u}^-_{i+1/2,j} = \bar{v}_{i,j} + \bar{m}(\bar{v}^-_{i+1/2,j} - \bar{v}_{i,j}, \bar{v}_{i,j} - \bar{v}_{i-1,j}, \bar{v}_{i+1,j} - \bar{v}_{i,j}), \tag{67}$$

$$\bar{u}^+_{i-1/2,j} = \bar{v}_{i,j} - \bar{m}(\bar{v}_{i,j} - \bar{v}^+_{i-1/2,j}, \bar{v}_{i,j} - \bar{v}_{i-1,j}, \bar{v}_{i+1,j} - \bar{v}_{i,j}). \tag{68}$$

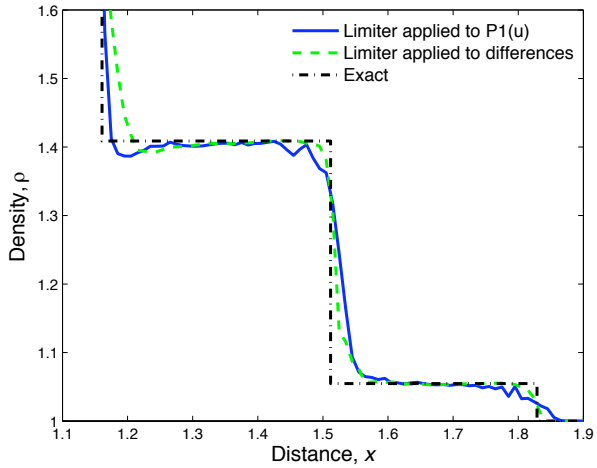

Figure 8: Density profiles from Torrihon's MHD shock tube problem at $t = 0.4$ from RKDG schemes using the HLLC-L flux solver and the LR limiter. Results are compared for the following cases: the necessity of limiting is detected using the P_1 projection of the solution; the necessity of limiting is detected using the difference between the element mean and edge mean values.

if $\bar{u}^-_{i,j+1/2} = \bar{u}^-_{i,j+1/2}$, $\bar{u}^+_{i,j-1/2} = \bar{u}^+_{i,j-1/2}$, $\bar{u}^-_{i+1/2,j} = \bar{u}^-_{i+1/2,j}$ and $\bar{u}^+_{i-1/2,j} = \bar{u}^+_{i-1/2,j}$, we assume that no limiting is required so,

$$u_h|E_{i,j} = v_h|E_{i,j}.$$

Otherwise $u_h|E_{i,j}$ is set to the limited P^1 part of $v_h|E_{i,j}$. This is computed by setting,

$$\bar{u}_{i,j} = \bar{v}_{i,j}, \tag{69}$$

$$u_x = \bar{m}(v^1_x, \bar{v}_{i,j} - \bar{v}_{i,j-1}, \bar{v}_{i,j+1} - \bar{v}_{i,j}), \tag{70}$$

$$u_y = \bar{m}(v^1_y, \bar{v}_{i,j} - \bar{v}_{i-1,j}, \bar{v}_{i+1,j} - \bar{v}_{i,j}), \tag{71}$$

for $E_{i,j}$.

6. Numerical Results

6.1. Simple Wave Problem

Landau and Lifshitz [43] present an exact, non-linear smooth solution to the one-dimensional Euler equations (no magnetic field). The solution only exists

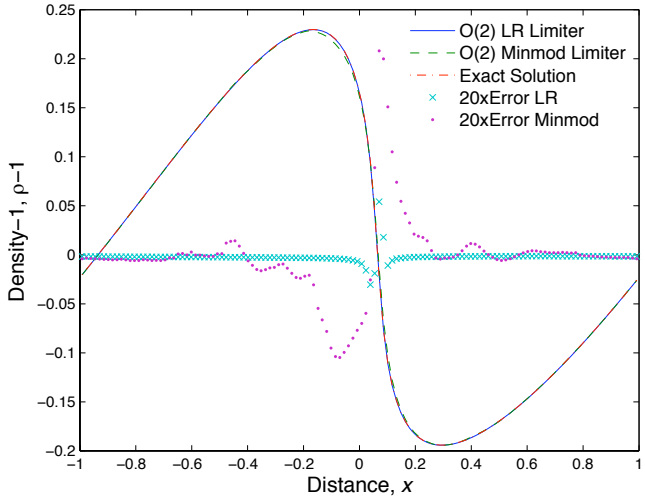

Figure 9: Solutions from second-order simulations of the Euler simple wave problem. The HLLC-L flux solver was used in all simulations shown. Twenty times the absolute error in each numerical solution is also plotted.

if the initial conditions satisfy the following relations:

$$\rho(x,0) = \rho_0 \left(1 + \frac{(\gamma-1)u_x}{2a_0}\right)^{\frac{2}{\gamma-1}},$$
$$p(x,0) = p_0 \left(1 + \frac{(\gamma-1)u_x}{2a_0}\right)^{\frac{2\gamma}{\gamma-1}},$$
$$u_y = u_z = B_x = B_y = B_z = 0.$$

The particular case we utilize has the initial velocity,

$$u_x(x,0) = u_0 \sin \pi x,$$

on the domain $-1 < x < 1$ with the boundary condition $u(1,t) = u(-1,t)$. The exact solution is initially smooth, but the sinusoidal waves steepen nonlinearly until a shock develops at t_{shock}, and the exact solution breaks down. The fact that the solution is smooth prior to t_{shock} implies that the numerical methods we are interested in testing should reproduce the solution to their theoretical order of accuracy, even though this is a nonlinear problem. This is not the case with any solution that involves discontinuities, such as a shock tube problem, because around discontinuities these methods revert to first-order accuracy. The existence of an exact solution to the Euler simple wave problem allows us to study the convergence of RKDG schemes for a nonlinear problem. We will

examine the results at $t = 0.9$, somewhat prior to the formation of a shock at $t \approx 0.95$.

In Fig. 9, the solution from limited second-order simulations are compared to the exact solution. The HLLC-L Riemann solver was used for both simulations. During the simulation, the less restrictive (LR) limiter did not detect that any limiting was required, thus it is unnecessary to show a separate curve for an unlimited simulation. On the other hand the minmod limiter detected that limiting was required on the majority of elements. This indicates a major short-coming of the minmod limiter for high-order simulations: The minmod limiter selects the input gradient with the minimum modulus. If this is not the gradient of the polynomial representation of the field internal to the element, then limiting is carried out and the coefficients of the higher order modes are set to zero. In the RKDG method, the input gradients are the internal gradient, and slope estimates based on the difference between the element average fields and the average fields on the adjacent elements. In general, if the solution has a finite curvature, the internal gradient will not have the minimum modulus, thus the solution will be limited and will revert to (at most) second order accuracy. This will occur even if limiting is unnecessary, as is the case with the solution we are currently examining. From this we must conclude that the minmod limiter is unsuited for use in a high-order RKDG method. Examining the numerical solutions shown in Fig. 9, we see that the LR limited solution approximates the exact solution very well, while the minmod limited solution slightly under-predicts the peak value.

In Fig. 10, we show how the L^2 error in element average density converges with N for various RKDG schemes. The least squares fitted order of convergence for each scheme is indicated in the figure legend. Note that in these simulations, the LR limiter does not detect that any limiting is required, so there is no need to present separate LR limited and unlimited results. The solutions from the LR limited third- and fourth-order RKDG schemes converge at the expected rate. On the other hand, the results from the minmod limited fourth-order RKDG scheme show an order of convergence of between one and two. This is due to the solution being limited to piecewise linear or piecewise constant on the majority of elements, once again highlighting the short-comings of this limiter.

To further investigate the importance of using accurate Riemann solvers in high-order schemes, in Fig. 10 we compare the convergence of solutions from LR limited third- and fourth-order RKDG schemes using LF and HLLC-L Riemann solvers. For the third-order scheme, the solutions produced using the HLLC-L solver have lower errors and converge more rapidly, as might have been anticipated from our low-order results. However, for the fourth-order scheme the errors in the LF and HLLC-L results are indistinguishable on the scale of the plot for all discretizations used. This shows that high-order accurate solutions to the simple wave problem are insensitive to the choice of Riemann solver over a broad range of resolutions, supporting the view of Cockburn and Shu [13], at least for smooth solutions.

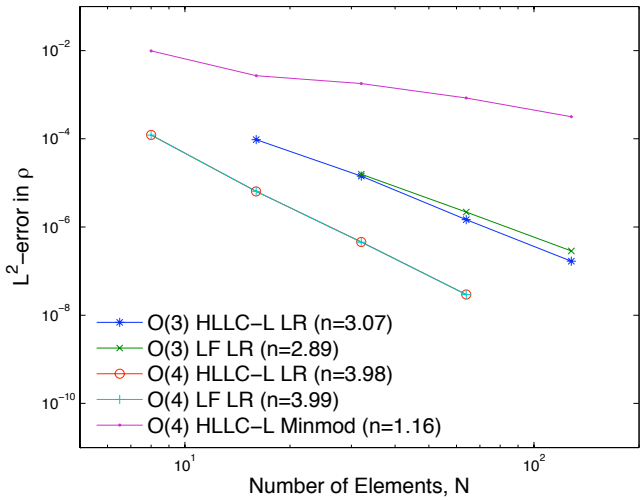

Figure 10: L^2 errors in element average density versus N for the Euler simple wave problem at $t = 0.5$. The least-squares fitted order of convergence, n, for each scheme is indicated in the legend.

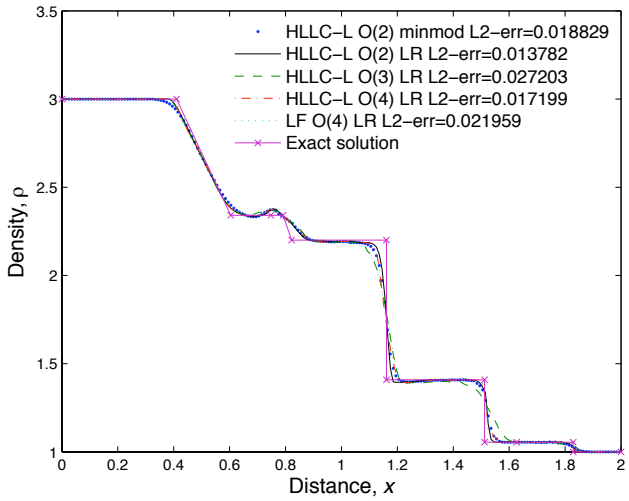

Figure 11: Numerical solutions to Torrilhon's Riemann problem at $t = 0.4$ using second- and third- and fourth-order RKDG schemes. The HLLC-L flux solver was used in all simulations other than one. A fourth-order result using the LF flux is shown for comparison. The L^2 error in the element average densities for each simulation is also indicated in the legend.

6.2. Behavior of Limited Solutions for Problems Dominated by Discontinuities

To investigate the effect of low-order limiting and accurate Riemann solvers in problems dominated by discontinuities, we compare numerical solutions to Torrilhon's MHD Riemann problem from second-, third- and fourth-order RKDG schemes. These are shown in Fig. 11. Let us first examine the impact of the Riemann solver on solutions from the LR limited fourth order scheme. When the LF flux is used the L^2-error in the element average density is 0.0220. Using the more accurate HLLC-L solver, this error is reduced to 0.0172, which is significant. This is in contrast to our earlier results for smooth solutions indicates that when discontinuities are present, the choice of Riemann solver *is* still significant for high-order methods. The reasons for this will become clear by the end of this discussion.

We now turn our attention to the results of differing order produced using the HLLC-L solver. From Fig. 11, we observe that the solution from the third-order scheme is the least accurate overall, with an L^2 error in the element average density of 0.0272. The behavior of the second- and fourth-order LR limited schemes is similar, other than in the vicinity of the contact discontinuity where the second-order scheme is more accurate. This results in the error in the solution from the fourth-order scheme (0.0172) being greater than that from the second-order scheme (0.0138). Both of these two solutions are more accurate than that from the minmod limited second-order scheme, which has a error of 0.0188.

The reason why we do not observe an increase in accuracy as the order of the scheme is increased, and why the LR limiting procedure results in more accurate solutions, can be explained by examining where the limiter functions alter the polynomial order of the solution. For $t = 0.4$, this is shown in Fig. 12 for LR and minmod limited second-order RKDG schemes, and in Fig. 13 for LR limited third- and fourth-order RKDG schemes. From Fig. 12, we see that in the second-order solution, the minmod limiter carries out limiting on almost all elements where the solution is non-constant, resulting in 117 of 200 elements being limited. The LR limiter limits far fewer elements, 32 of 200 in this example, mostly those on the edge of discontinuities. This results in the minmod limited solution being more diffuse than the LR limited solution, as can be seen in Fig. 11, and therefore less accurate, as the L^2 errors revealed. From Fig. 13, we see that 43 and 56 elements are limited to lower order polynomials in the solutions from the LR limited third- and fourth-order schemes, respectively. Also, the unlimited elements are in general located where the solution is close to linear, so that a higher-order representation of the data has little impact on the overall accuracy of the solution. The cumulative result is that the error caused by additional limiting outweighs any gain in accuracy due to the increased order of the scheme, resulting in the third- and fourth-order schemes producing less accurate solutions than the LR limited second-order scheme. For this discontinuity dominated problem, these results indicate that if elements are limited to a maximum polynomial order of one, and the overall scheme is at least second-order accurate, then the L^2 error in the solution is influenced

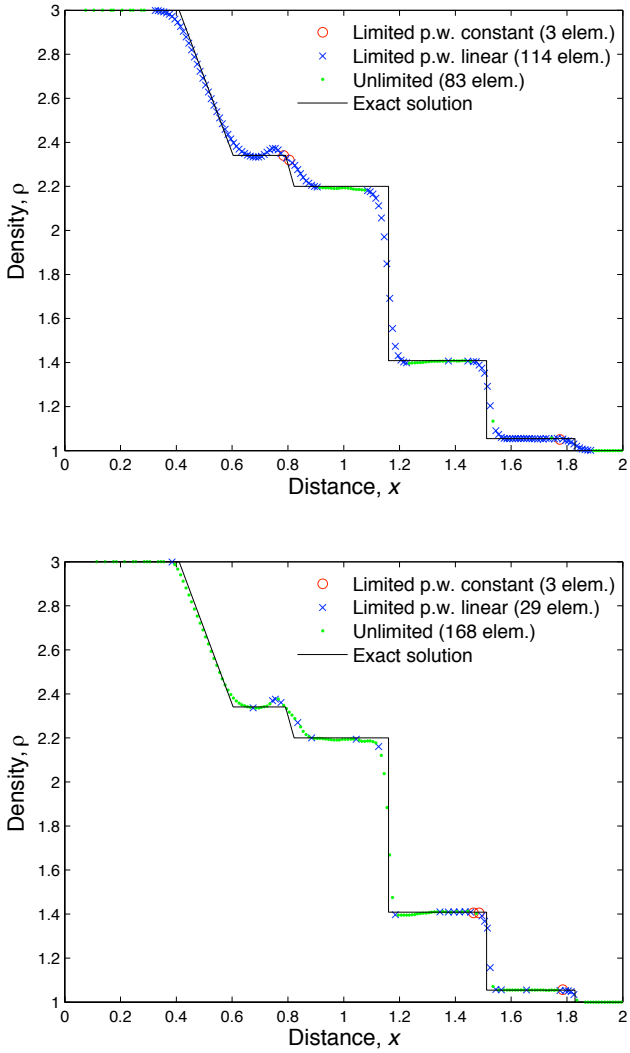

Figure 12: Distribution of limited elements in solutions to Torrilhon's MHD Riemann problem at $t = 0.4$ from second-order RKDG schemes. The HLLC-L flux solver was used along with the minmod (top) and LR (bottom) limiters.

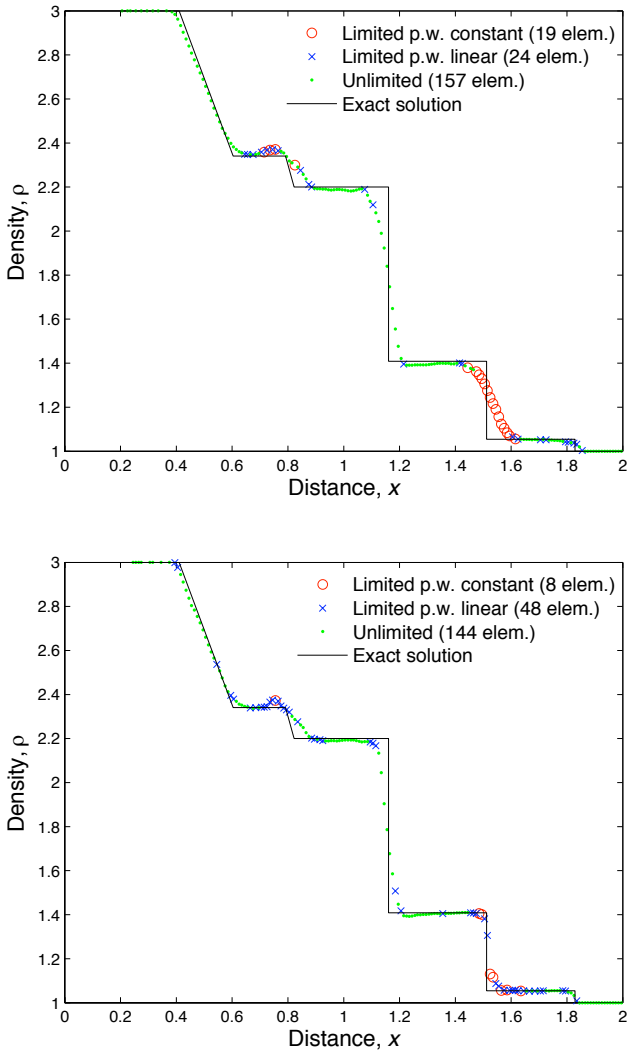

Figure 13: Distribution of limited elements in solutions to Torrilhon's MHD Riemann problem at $t = 0.4$ from third-order (top) and fourth-order (bottom) RKDG schemes. The HLLC-L flux solver was used along with the LR limiter.

more by the extent to which the solution must be limited than by the order of accuracy of the scheme.

The remaining issue to be addressed from the results shown in Fig. 12 and Fig. 13 is why the third-order scheme produces the solution with the largest L^2 error in element average densities. The reason appears to be that the limiter function interacts poorly with the piecewise quadratic representation of the data, in that it limits the data to be piecewise constant on a far greater number of elements than for the other schemes, which locally reduces the order of the scheme to one. It is important to note that the distributions of limited elements shown in Fig. 13 are instantaneous. These distributions change significantly with time. In particular, the third-order scheme was observed to require limiting on a far greater number of elements after the first and second sub-steps of the RK scheme than after the third and final sub-step, which is what we see in Fig. 13. For example after the second sub-step at $t = 0.4$, the solution is limited to piecewise constants on 27 elements and piecewise linear functions on 29 elements. The fact that the scheme is reduced to first-order on this number of elements results in the solution it produces being less accurate than even the second-order minmod limited solution.

In conclusion, for high-order RKDG simulations of Torrilhon's MHD Riemann problem, the polynomial representation of the data is limited to be at most piecewise linear around the discontinuities. The remaining elements where the representation is piecewise quadratic (for third-order) or cubic (for fourth-order) lie in regions where the exact solution is linear and would thus be represented equally well by a lower-order function. This implies that, at best, a high-order RKDG scheme will behave in the same manner as a second-order scheme for the problem studied here. The only remedy for this would be to develop a limiter function that produces higher-order limited polynomials. Our results imply that for any problem featuring by discontinuities, the error in a solution produced by a high-order RKDG method is likely to be dominated by the low-order errors in the vicinity of the discontinuities. Such errors have been show to be significantly reduced by the use of accurate Riemann solvers in Section 4.2. This explains the improved performance of the fourth-order scheme when the HLLC-L solver was used instead of the LF flux.

6.3. Orzag-Tang Vortex

To verify that our findings hold in multiple dimensions, we examine simulations of the Orzag-Tang vortex [44], a commonly used multi-dimensional test case for ideal MHD solvers (see e.g. [45], [30]). The problem is very cleanly defined with periodic boundary conditions in both directions. The domain for this test case is $0 < x,\ y < 2\pi$, $0 \leq t \leq \pi$, and the initial conditions are,

$$(\rho,\, p,\, u,\, v,\, w,\, B_x,\, B_y,\, B_z) = (\gamma^2,\, \gamma,\, -\sin y,\, \sin x,\, 0,\, -\sin y,\, \sin 2x,\, 0).$$

The problem is solved for an ideal plasma with $\gamma = 5/3$.

We present solutions from fourth-order RKDG simulations using the LF and HLLC-L fluxes, along with a high resolution reference solution. The RKDG

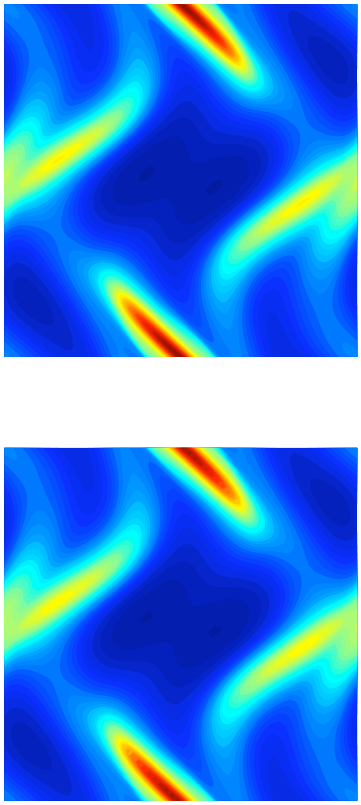

Figure 14: Density distribution at $t = 0.8$ from a second-order finite volume scheme on a 256 by 256 cell regular mesh (top) and a fourth-order RKDG scheme on a 64 by 64 element regular mesh (bottom). The HLLC-L flux solver was used along with the LR limiter in the RKDG scheme. The same contour levels are used in both plots.

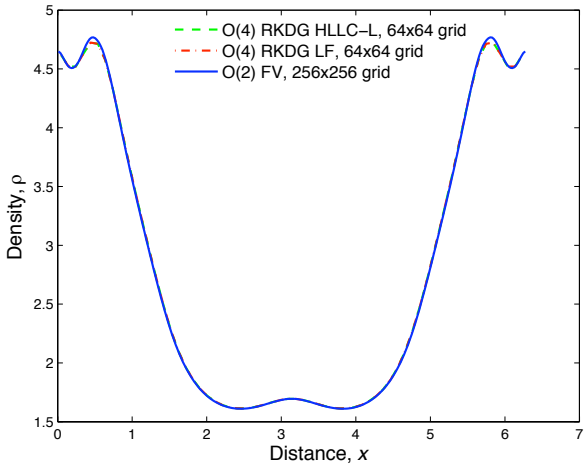

Figure 15: Density profiles at $t = 0.8$, $y = \pi$ from a second-order finite volume scheme on a 256 by 256 cell regular mesh and a fourth-order RKDG scheme on a 64 by 64 element regular mesh. The HLLC-L flux solver was used along with the LR limiter in the RKDG scheme.

simulations were run on a relatively coarse regular grid of 64 by 64 elements. The method of Powell et al. [37] is used to control divergence errors in the magnetic field. The high resolution reference solution is required because an exact solution to this test case does not exist. It was produced using a second-order accurate finite volume scheme on a 256 by 256 cell regular grid. The finite volume scheme was developed by Samtaney [46] and uses the 8-wave upwinding formulation of Powell et al. [37] within an unsplit upwinding method [47]. The solenoidal property of the magnetic field is enforced at each time step using a projection method. A constrained transport step is then used remove divergence modes with a centered finite difference representation. This uses the formulation prescribed by Toth [48].

During the early development of the vortex, the flow is smooth and limiting is not required. Fig. 14 shows density fields from the RKDG and reference solutions at $t = 0.8$, when the solution is still smooth. Only one RKDG solution is shown as the difference between them is negligible. From Fig. 14 we see that there is excellent agreement between the RKDG and reference solutions, indicating that the method performs well when limiting is not required. To show the differences between the solutions more clearly, we show the density profiles along the line $y = \pi$ in Fig. 15. The only visible deviation of the lower resolution RKDG simulations from the reference solution is a slight under-prediction of the peak density. The RKDG results using the LF and HLLC-L fluxes cannot be distinguished on the scale of this plot. This indicates that as in one-dimension, the results or high-order RKDG simulations of smooth solutions are insensitive

to the choice of Riemann solver.

Fig. 16 shows density fields at $t = \pi$ from the RKDG simulation that used the HLLC-L flux and the reference solution. By this time, the flow has evolved into a complex state featuring numerous discontinuities. At this stage there is a need for extensive limiting, with approximately 37% and 33% of the elements being limited in the RKDG simulations using the HLLC-L and LF fluxes, respectively. Comparing the reference solution and the RKDG solution shown in Fig. 16, it can be seen that the while the overall shock structure is the similar in both simulations, the RKDG result is far more diffuse. In fact many of the fine scale features are not adequately resolved. To show this more clearly, we show the density profiles from all simulations along the line $y = \pi$ in Fig. 17. From the figure we see that the RKDG solutions fail to capture the sharp peaks in density, along with the sharp trough in the center of the domain. This is due to the extensive limiting causing the scheme to revert to at most second-order accuracy in these regions around the discontinuities. As for the one-dimensional discontinuous flows studied in the previous subsection, the choice of Riemann solvers now significantly affects the RKDG solutions. From Fig. 17 it can be seen that the more accurate HLLC-L solver allows the scheme to better resolve the features in the center of the domain.

7. Conclusions

To investigate the importance of accurate Riemann solvers in RKDG simulations, we examined the results of first-, second-, third-, and fourth-order simulations of both smooth and non-smooth problems. In the presence of discontinuities, the influence of Riemann solver selection is directly tied to the performance of limiters. Thus we also examined the performance of common limiters in these simulations. It was noted that a particular extension of one-dimensional limiters to multiple dimensions can result in the TVD condition being violated.

We first examined the computational efficiency of several recently developed MHD Riemann solvers, in terms of the computing time required to achieve a fixed error bound for a given problem. The performance of these solvers was compared to that of the Roe solver, the LF flux and the MHD HLLE-M solver, which had previously been identified as the most efficient by Wesenberg [25]. This was done for first- and second-order schemes. We find that all of the accurate Riemann solvers are more computationally efficient than the LF flux, with the HLLE-M, HLLC-L, HLLD and Roe solvers exhibiting similar efficiency. The HLLD and HLLC-L solvers were identified as good candidates for use in high-order simulations as of the most efficient group of solvers, these have the most desirable robustness properties.

From our third- and fourth-order results for smooth solutions, we conclude that the minmod limiter is unsuited for use in high-order RKDG methods. The reason for this is that in regions of finite curvature, this limiter tends to restrict the polynomial order of the trial space, reducing the scheme to at most second-order accuracy, even when limiting is not strictly required to keep the scheme

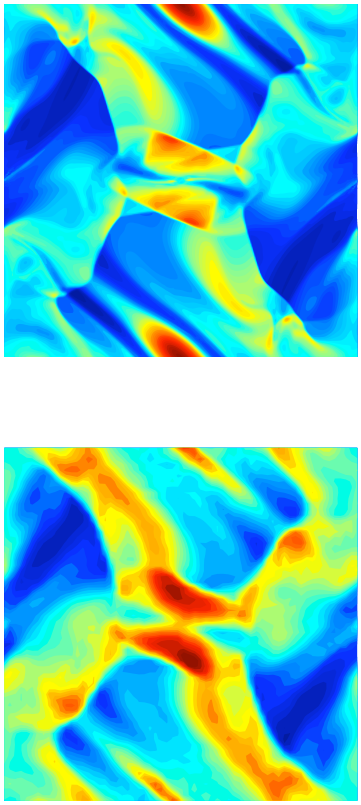

Figure 16: Density distribution at $t = \pi$ from a second-order finite volume scheme on a 256 by 256 cell regular mesh (top) and a fourth-order RKDG scheme on a 64 by 64 element regular mesh (bottom). The HLLC-L flux solver was used along with the LR limiter in the RKDG scheme. The same contour levels are used in both plots.

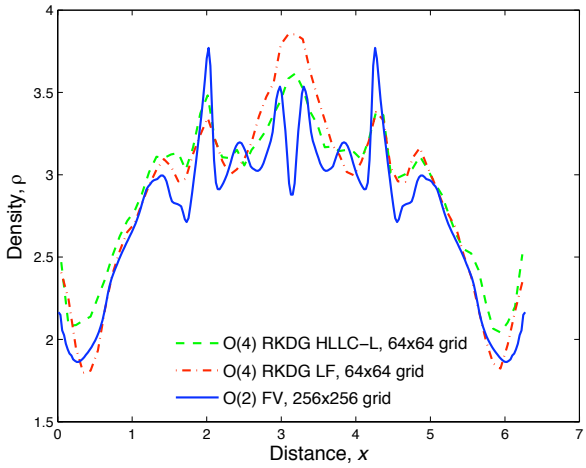

Figure 17: Density profiles at $t = \pi$, $y = \pi$ from a second-order finite volume scheme on a 256 by 256 cell regular mesh and a fourth-order RKDG scheme on a 64 by 64 element regular mesh. The HLLC-L flux solver was used along with the LR limiter in the RKDG scheme.

TVD. The less-restrictive limiter does not exhibit this behavior. For third-order simulations of smooth problems, we find that using the HLLC-L solver results in lower errors and faster convergence than when the LF flux is used. However, for fourth-order simulations of the same problem, we observe negligible differences in the solutions when the Riemann solver is varied. This supports the view of Cockburn and Shu [13] that the results of high-order RKDG simulations are insensitive to the choice of Riemann solver, at least for smooth solutions.

From our simulations of problems dominated by discontinuities, we find that in the vicinity of discontinuities, high-order RKDG methods behave in a similar manner to the second-order method due to the use of a piecewise linear limiter. The error in numerical solutions to such problems is dominated by the error in these regions. Thus, for such solutions, the choice of Riemann solver used in a high-order method has a similar significance as for a second-order method. Our analysis of second-order methods indicates that the choice of Riemann solvers is very significant, with the more accurate Riemann solvers having the best performance. This results in fourth-order simulations of discontinuous solutions using the HLLC-L solver having considerably lower error than those using the LF flux, in contrast to the result for smooth solutions.

References

[1] D. J. Hill, D. I. Pullin, Hybrid tuned center-difference-WENO method for large eddy simulations in the presence of strong shocks, J. Comp. Phys.

194 (2004) 435–450.

[2] T. R. Hill, W. H. Reed, Triangular mesh methods for neutron transport equation, Tech. Rep. LA-UR-73-479, Los Alamos Scientific Laboratory, 1973.

[3] P. LeSaint, P. A. Raviart, On a finite element method for solving neutron transport euqation, Mathematical aspects of finite element in partial differential equations (C. de Boor, Ed.), Academics Press (1974) 89–145.

[4] C. Johnson, J. Pitkaranta, An analysis of discontinuous Galerkin method for scalar hyperbolic equation, Math. Comp. 46 (1986) 1–26.

[5] T. Peterson, A note on the convergence of discontinuous Galerkin method for a scalar hyperbolic equation, SIAM J. Numer. Anal. 28 (1991) 133–140.

[6] S. Cockburn, B. Hou, C. W. Shu, The Runge-Kutta local projection discontinuous Galerkin finite element method for conservation laws IV: the multidimensional case, Math. Comp. 54 (1990) 545–581.

[7] S. Y. Cockburn, B. Lin, C. W. Shu, TVB Runge-Kutta local projection discontinuous Galerkin finite element method for conservation laws III:one dimensional systems, J. Comput. Phys. 84 (1989) 90–113.

[8] B. Cockburn, C. W. Shu, TVB Runge-Kutta local projection discontinuous Galerkin finite element method for conservation laws II:general framework, Math. Comp. 52 (1989) 411–435.

[9] B. Cockburn, C. W. Shu, The Runge-Kutta local projection P1-discontinuous Galerkin finite element method for scalar conservation laws, Math. Model. Numer. Anal. (M^2AN) 25 (1991) 337–361.

[10] B. Cockburn, C. W. Shu, The Runge-Kutta local projection discontinuous Galerkin finite element method for conservation laws V: the multidimensional systems case, J. Comput. Phys. 141 (1998) 199–224.

[11] G. Chavent, B. Cockburn, The local projection p^0 p^1-discontinuous Galerkin finite element method for scalar conservation law, Math. Model. Numer. Anal. (M^2AN) 23 (1989) 565–592.

[12] C. W. Shu, S. Osher, Efficient implementation of essentially non-oscillatory shock capturing schemes, J. Comput. Phys. 77 (1988) 439–471.

[13] B. Cockburn, C. W. Shu, Runge-Kutta Discontinuous Galerkin Methods for Convection-Dominated Problems, J. Sci. Comp. 16 (2001) 173–261.

[14] J. X. Qiu, B. C. Khoo, C. W. Shu, A numerical study for the performance of the Runge-Kutta discontinuous Galerkin method based on different numerical fluxes, J. Comput. Phys. 212 (2006) 540–565.

[15] A. Harten, P. D. Lax, B. van Leer, On upstream differencing and Godunov-type methods for hyperbolic conservation laws, SIAM Rev. 25 (1983) 35.

[16] E. F. Toro, M. Spruce, W. Speares, Restoration of the contact surface in the HartenLaxvan Leer Riemann solver, J. Shock Waves 4 (1994) 25–34.

[17] V. A. Titarev, E. F. Toro, Finite-volume WENO schemes for three-dimensional conservation laws, J. Comput. Phys. 201 (2004) 238–260.

[18] G. W. Sutton, A. Sherman, Engineering Magnetohydrodynamics, McGraw-Hill, 1965.

[19] S. J. Sherwin, G. E. Karniadakis, A new triangular and tetrahedral basis for high-order finite element methods, Int. J. Numer. Methods. Eng. 123 (1995) 3775.

[20] M. Dubiner, Spectral methods on triangles and other domains, J. Sci. Comp. 6 (1991) 345.

[21] T. C. Warburton, G. E. Karniadakis, A Discontinuous Galerkin Method for the Viscous MHD Equations, J. Comp. Phys. 152 (1999) 608–641.

[22] C. W. Shu, Total-Variation-Diminishing time discretizations, SIAM J. Sci. and Stat. Comput. 9 (1988) 1073–1084.

[23] B. Cockburn, C. W. Shu, The Runge-Kutta local projection p^1-discontinuous Galerkin finite element method for scalar conservation laws, M^2AN 25 (1991) 337–361.

[24] B. Cockburn, Advanced Numerical Approximation of Nonlinear Hyperbolic Equations, chap. An introduction to the Discontinuous Galerkin method for convection-dominated problems, Lecture Notes in Mathematics, Springer, 151–268, 1998.

[25] M. Wesenberg, Efficient MHD Riemann solvers for simulations on unstructured triangular grids, J. Numer. Math. 10 (2002) 37–71.

[26] P. Janhunen, A positive conservative method for magnetohydrodynamics based on HLL and Roe methods, J. Comput. Phys. 160 (2000) 649–661.

[27] T. Linde, A practical, general-purpose, two-state HLL Riemann solver for hyperbolic conservation laws, Int. J. Numer. Meth. Fluids 40 (2002) 391–402.

[28] S. Li, An HLLC Riemann solver for magneto-hydrodynamics, J. Comp. Phys. 203 (2005) 344.

[29] K. F. Gurski, An HLLC-type approximate Riemann solver for ideal magnetohydrodynamics, SIAM J. Sci. Comp. 25 (2004) 2165.

[30] T. Miyoshi, K. Kusano, A multi-state HLL approximate Riemann solver for ideal magnetohydrodynamics, J. Comp. Phys. 208 (2005) 315–344.

[31] D. Ryu, T. W. Jones, Numerical magnetohydrodynamics in astrophysics: algorithm and tests for one-dimensional flow, Astrophys. J. 442 (1995) 228.

[32] B. Einfeldt, C. D. Munz, P. L. Roe, B. Sjögreen, On Godunov-type methods near low densities, J. Comp. Phys. 92 (1991) 273.

[33] K. F. Gurski, A Comparison of Two Intermediate State HLLC Solvers for Ideal Magnetohydrodynamics, in: N. V. Porelov, E. Audit, G. P. Zank (Eds.), Numerical Modeling of Space Plasma Flows: Astronum 2007, vol. 385 of *ASP Conference Series*, 341–348, 2008.

[34] M. Brio, C. C. Wu, An Upwind Differencing Scheme for the Equations of Ideal Magnetohydrodynamics, J. Comp. Phys. 75 (1988) 400–422.

[35] P. Cargo, G. Gallice, Roe matrices for ideal MHD and systematic construction of Roe matrices for systems of conservation laws, J. Comp. Phys. 136 (1997) 446.

[36] D. S. Balsara, Linearized formulation of the Riemann problem for adiabatic and isothermal magnetohydrodynamics, Astrophys. J. Supp. 116 (1998) 119.

[37] K. G. Powell, P. L. Roe, T. J. Linde, T. I. Gombosi, D. L. DeZeeuw, A solution-adaptive upwind scheme for ideal magnetohydrodynamics, J. Comp. Phys. 154 (1999) 284–309.

[38] S. F. Davis, Simplified second-order Godunov-type, SIAM J. Sci. Statist. Comput. 9 (1988) 445.

[39] M. Torrilhon, Non-uniform convergence of finite volume schemes for Riemann problems of ideal magnetohydrodynamics, J. Comp. Phys. 192 (2003) 73–94.

[40] S. A. E. G. Falle, S. S. Komissarov, On the inadmissibility of non-evolutionary shocks, J. Plasma Physics 65 (1) (2001) 29–58.

[41] J. J. Quirk, A contribution to the great Riemann solver debate, Int. J. Num. Meth. Fluids 18 (1994) 555.

[42] C. W. Shu, TVB uniformly high order schemes for conservation laws, Math. Comp. 49 (1987) 105–121.

[43] L. D. Landau, E. M. Lifshitz, Fluid Mechanic, chap. 101, Butterworth-Heinemann, 2 edn., 378, 1987.

[44] A. Orzag, C. M. Tang, Small-scale structure of two-dimensional magneto-hydrodynamic turbulence, J. Fluid Mech. 90 (1979) 129.

[45] G. Toth, The $\nabla \cdot \mathbf{B}$ Constraint in Shock-Capturing Magnetohydrodynamics Codes, J. Comp. Phys 161 (2000) 605–652.

[46] R. Samtaney, Suppression of the Richtmyer-Meshkov instability in the presence of a magnetic field, Physics of Fluids 15 (8) (2003) L53–L56.

[47] P. Colella, Multidimensional upwind methods for hyperbolic conservation laws, J. Comp. Phys. 87 (1990) 171–200.

[48] G. Toth, The $\nabla \cdot B = 0$ constraint in shock-capturing magnetohydrodynamics codes, J. Comput. Phys. 161 (2000) 2605–2652.

Research Reports

No.	Authors/Title
09-39	*V. Wheatley, P. Huguenot, H. Kumar* On the role of Riemann solvers in discontinuous Galerkin methods for magnetohydrodynamics
09-38	*E. Kokiopoulou, D. Kressner, N. Paragios, P. Frossard* Globally optimal volume registration using DC programming
09-37	*F.G. Fuchs, A.D. McMurray, S. Mishra, N.H. Risebrom, K. Waagan* Approximate Riemann solvers and stable high-order finite volume schemes for multi-dimensional ideal MHD
09-36	*Ph. LeFloch, S. Mishra* Kinetic functions in magnetohydrodynamics with resistivity and hall effects
09-35	*U.S. Fjordholm, S. Mishra* Vorticity preserving finite volume schemes for the shallow water equations
09-34	*S. Mishra, E. Tadmor* Potential based constraint preserving genuinely multi-dimensional schemes for systems of conservation laws
09-33	*S. Mishra, E. Tadmor* Constraint preserving schemes using potential-based fluxes. III. Genuinely multi-dimensional central schemes for for MHD equations
09-32	*S. Mishra, E. Tadmor* Constraint preserving schemes using potential-based fluxes. II. Genuinely multi-dimensional central schemes for systems of conservation laws
09-31	*S. Mishra, E. Tadmor* Constraint preserving schemes using potential-based fluxes. I. Multidimensional transport equations
09-30	*D. Braess, S. Sauter, C. Schwab* On the justification of plate models
09-29	*D. Schötzau, C. Schwab, T. Wihler* *hp*-dGFEM for second-order elliptic problems in polyhedra. II: Exponential convergence
09-28	*D. Schötzau, C. Schwab, T. Wihler* *hp*-dGFEM for second-order elliptic problems in polyhedra. I: Stability and quasioptimality on geometric meshes
09-27	*A. Moiola, R. Hiptmair, I. Perugia* Approximation by plane waves